A phase field model for partially saturated geomaterials describing fluid-fluid displacements. Part I: The model and one-dimensional analysis

Siddhartha Ommi, Giulio Sciarra, Panagiotis Kotronis

Advances in Water Resources 164 (2022) 104170

Contents lists available at ScienceDirect

Advances in Water Resources

journal homepage: www.elsevier.com/locate/advwatres

A phase field model for partially saturated geomaterials describing fluid–fluid displacements. Part I: The model and one-dimensional analysis

Siddhartha H. Ommi *, Giulio Sciarra, Panagiotis Kotronis

Nantes Université, Ecole Centrale Nantes, CNRS, GeM, UMR 6183, F-44000, Nantes, France

ARTICLE INFO

Keywords:
Partial saturation
Imbibition
Drainage
Phase field modeling

ABSTRACT

A model describing immiscible fluid–fluid displacements in partially saturated porous media is presented. This is based on a phase field approach that interprets the mixture of wetting (liquid water) and non-wetting (air) fluids within the pore space as a single saturating non-uniform pore fluid characterized by a phase field parameter, which is considered to be the saturation degree of the wetting fluid. While the standard retention curve provides for the retention properties of the pore walls, a Cahn–Hilliard like double-well energy is employed to describe the possible co-existence of the immiscible fluid phases. An enhanced description of the macroscopic surface tension between the fluid phases is obtained naturally within the phase field framework due to a regularization that depends on the spatial gradient of the water content. A generalized Darcy's law is used to describe dissipation due to fluid flow driven by the gradient of a generalized chemical potential. Thus, in the context of soil hydrology this model is interpreted as an extension to the classical Richards equation governing the spatio-temporal evolution of the phase field parameter. Employing a convex–concave flux function it is shown, using one-dimensional analysis, that both imbibition and drainage fronts can be modeled in this phase field framework. The non-monotonicities observed in the resolved solutions are explained using a combination of asymptotic matching techniques and dynamical systems analysis.

1. Introduction

Stability of a moving interface between two immiscible fluids of contrasting viscosities and densities is a classical problem in fluid mechanics. Further when a solid substrate is involved the problem becomes more complex with the addition of wettability of the solid surface with respect to the fluid combination. This is almost always the case when two fluids are involved such as in the Hele-Shaw flow and in multi-phase flow in porous media such as soils. Being able to model the displacement of such interfaces has its uses in a myriad of applications ranging from hydrology to Carbon dioxide (CO_2) sequestration. In hydrology, when water infiltrates into soil while displacing air, the stability of the interface plays a consequential role in the transport of solutes and contaminants to the ground waters (Glass et al., 1988; Jarvis, 2007; Clothier et al., 2008). In fact soil layers filter the rain waters before they reach the water table and this can be impacted negatively by the formation of preferential pathways due to unstable infiltration. Sequestration of CO_2 is a key part of carbon capture and storage (CCS) as a solution to counter the mounting accumulation of atmospheric greenhouse gasses (Lackner, 2003; Torp and Gale, 2004; Orr, 2004; Ajayi et al., 2019). This process involves injection of compressed CO_2 while displacing the resident wetting fluid (usually water or oil) in high permeable aquifer rock formations at suitable geological sites such as depleting oil or gas fields, deep saline formations and unmineable coal seams. A low permeable cap-rock usually acts as a natural barrier to trap the injected CO_2. Any instability relative to an advancing interface within this layer leads to reduced efficiency of the operation (Yamabe et al., 2015; Zacharoudiou et al., 2018). It can even pose an environmental risk if preferential paths are triggered by the fault planes in the cap-rock thus providing an escape route to the rising or migrating CO_2 plumes (Macminn et al., 2010; Gilfillan et al., 2011; Song and Zhang, 2013).

When the resident/defending fluid preferentially wets the solid substrate the displacement of it by a non-wetting fluid is termed as drainage. The contrary is termed imbibition, when the invading fluid is wetting. In both these scenarios, numerous experimental campaigns have been carried out by various researchers with an intent to characterize the unstable displacement and the ensuing pattern formation. One can refer to the seminal works of Lenormand and his colleagues in the 1980s (Lenormand, 1985; Lenormand et al., 1988; Lenormand, 1990) and the other researchers who followed this path. See Chen et al. (2017), Guo and Aryana (2019), to name a few.

* Corresponding author.
E-mail address: siddhartha-harsha.ommi@ec-nantes.fr (S.H. Ommi).

https://doi.org/10.1016/j.advwatres.2022.104170
Received 22 October 2021; Received in revised form 27 January 2022; Accepted 18 March 2022
Available online 4 April 2022

In more recent works such as Méheust et al. (2002), Løvoll et al. (2005), gravity has been shown to stabilize the invasion of a less dense non-wetting fluid into a porous medium that is saturated with more viscous and denser wetting fluid. On the contrary, when a denser and more viscous wetting fluid displaces a resident non-wetting fluid, the viscosity contrast is not in favor of destabilization (Saffman and Taylor, 1958; Homsy, 1987) and gravity is expected to assist in destabilizing the flow. This latter regime was the focus and a well-engaged topic of research in soil hydrology since the 1970s. One can look into DiCarlo (2013), Xiong (2014) among others for a review of gravity driven infiltration of water into soil. Experimental evidence in this context suggested that fingering type instabilities that occur during infiltration have a non-monotonic profile along their length, with their tips having higher water content compared to their tails. This observation and related numerical studies (Nieber et al., 2000; Eliassi and Glass, 2001) have lead to the hypothesis that this non-monotonicity is the cause rather than the consequence of the ensuing instability (Eliassi and Glass, 2001). This 'overshoot' of water content has been further evidenced experimentally to be present during two-dimensional (Bauters et al., 2000; Shiozawa and Fujimaki, 2004) and quasi one-dimensional (DiCarlo, 2004; DiCarlo et al., 2010) experiments with transverse domain size smaller than the finger size expected.

Now coming to the modeling efforts, the various methodologies that have been developed over the years for modeling flow in porous media can be broadly classified based on the spatial scale of the problem being tackled. The pore-scale network models such as the (Glass and Yarrington, 1996; Glass et al., 1998; Hughes and Blunt, 2000, 2001; Al-Gharbi and Blunt, 2005; Primkulov et al., 2018, 2019) and lattice-Boltzmann methods (Liu et al., 2012, 2014; Zhao et al., 2016) are interesting in studying the effect of rather intricate processes such as pore invasion, flow-by-film and formation of capillary bridges among others. Also, these methods were rather successful in describing regime transitions in the phase diagram (Lenormand, 1990) classifying the morphology of the fluid displacement. However, these approaches tend to quickly become non-viable for large scale practical applications. On the other hand macroscopic scale continuum modeling has proven to be a reliable tool to model laboratory scale and field scale problems. The most widely accepted continuum model for describing partially imbibed soils in hydrology is the now classical Richards equation (Richards, 1931) that is derived, under various assumptions (Hilfer and Steinle, 2014), from the conservation of fluid mass and the Darcy–Buckingham equation (Buckingham, 1907; Bear, 1972) that relates the pressure gradient to the fluid flux in an unsaturated porous medium. While this approach has been widely accepted, it suffered criticism over the years primarily due to the rough up-scaling law that is involved to model the retention effect of the pore walls on the fluids (Morrow, 1970). Secondly, due to its inability to reproduce physically observed fingering phenomenon (Egorov et al., 2003; Nieber et al., 2005). Various proposals have been done over the years to remedy these drawbacks, each one building on the existing structure of the Richards equation.

In the current study we propose a non-local extension to the Richards equation which is based on a more general framework (Sciarra, 2016) of thermodynamically consistent phase field modeling. At the core of this approach is the inspiration from the now classical Cahn–Hilliard (Cahn and Hilliard, 1958, 1959) modeling of multi-phase fluids involving phase segregation and diffused description of interfaces between the phases. The proposed approach is analyzed in detail in one-dimension portraying its ability to describe experimentally observed non-monotonic profiles of saturation in gravity driven infiltration and their link to the specific form of the energy employed. Another significant novelty of this work is the modeling of drainage fronts, besides imbibition, realized in the context of continuum poromechanics without falling-back on modeling hysteretic effects. This is done thanks to the presence of a non-local gradient energy contribution and by employing a non-convex flux function that drives the flow under the influence of an imposed uniform pressure gradient or an equivalent uniform bulk force. Such description of flux functions driving the flow are prevalent in thin film flows (Bertozzi et al., 1999; Münch, 2000), fractional flow formulations (DiCarlo et al., 2012; Hilfer and Steinle, 2014) among others. Our purpose being in formulating an enriched continuum model whose characteristic parameters could be, in principle, directly identified from experimental evidence, no comparison has been proposed with lattice-Boltzmann methods or other numerical schemes based on the premise that the macroscopic behavior of a fluid is the result of the average behavior of many microscopic particles in the system. The interested reader can for instance refer to Chen and Doolen (1998) and cited works within.

The one-dimensional solutions and the analysis thereof sets the stage for Part II of this work, where we show that two-dimensional imbibition and drainage solutions are conditionally stable to transverse perturbations, thus being able to generate fingering type instabilities.

This work is organized as follows: In Section 2 the Richards equation is introduced along with a brief review of its drawbacks and the existing extended models. Then the proposed model is presented recalling, from Sciarra (2016), the aspects of energy contributions and its roots to fundamental principles. The governing equation for saturation degree of wetting fluid is derived employing a generalized Darcy's law. In Section 3 a one-dimensional analysis is done employing a non-convex flux function followed by a traveling wave analysis and numerical resolution of the one-dimensional solutions. The conclusions are presented in Section 4.

The physical dimensions of quantities are mentioned whenever relevant alongside the corresponding symbols and within square brackets, $[\mathrm{M}^{(\cdot)}\ \mathrm{L}^{(\cdot)}\ \mathrm{T}^{(\cdot)}\ \Theta^{(\cdot)}]$. In Table 1 one can find the main symbols and their nomenclature adopted in this work. Note that some of the physical quantities with dimensions are rendered dimensionless, [–], according to the scheme presented within.

2. Mathematical model

The starting point of the current development is the classical poromechanical approach, see Coussy (2004, 2010), along with an overarching assumption of a rigid hydrophilic porous skeleton whose pore spaces are filled with two fluids, air and water. Now, due to the immiscibility of the fluids involved, triple lines arise at the pore-scale, when the air–water interfaces meet the pore walls. The motion of these triple lines governs the individual energy contributions of the interfaces formed among the solid, wetting and non-wetting fluids. The essence of the current work is two fold: to account for these interfacial energy contributions in a way that enriches the classical prescription allowing in particular for describing pinching and coalescence of fluid phases within the porous medium and secondly to shed light on the possibility of modeling both imbibition and drainage while adhering to the thermodynamic restrictions of a dissipative extended Darcy flow.

2.1. Classical approach

At the pore-scale, the menisci formed between the wetting and non-wetting fluids have certain curvature depending on the surface tension between the two fluids, their wettability with respect to the pore walls and the geometry of the pores. The pressure difference between the two fluids, that is the pore-scale capillary pressure, governs the volume fractions of those fluids within the pore space. Classical poromechanical practice involves assuming a simplistic geometry of the pore space and specifying that the work done by the pore-scale capillary pressure in causing infinitesimal variation in the volume content of the wetting fluid occupying the pore, is equivalent to the infinitesimal variation of interfacial energy (Coussy, 2010). Thus a continuum scale constitutive relation is determined between the interfacial energy, $U(S_w)$, and the saturation degree of the wetting fluid, S_w, i.e., the volume fraction of wetting fluid within the available pore space. This relation allows, at equilibrium, for retention of a given volume of wetting fluid at a

Table 1
List of main symbols and nomenclature.

Symbols	*Nomenclature*	*Dimensions (when applicable)*
t	physical time	[T]
x	coordinate in the physical space along x-direction	[L]
e_x	unit vector in the positive x-direction	[–]
∇	multi-dimensional gradient operator in the physical space	[L^{-1}]
$\nabla\cdot$	multi-dimensional divergence operator in the physical space	[L^{-1}]
$(\,)\cdot(\,)$	dot product between two vectors	
g	magnitude of gravitational acceleration	[LT^{-2}]
ρ_w, ρ_{nw}	intrinsic mass densities of wetting and non-wetting fluids respectively	[ML^{-3}]
S_w, S_{nw}	saturation degrees of wetting and non-wetting fluids respectively	[–]
p_w, p_{nw}	pressures of wetting and non-wetting fluids respectively	[$ML^{-1}T^{-2}$]
ϕ_0, ϕ	initial and Lagrangian porosities of the porous skeleton respectively	[–]
$\varkappa$	intrinsic permeability of the porous skeleton	[L^2]
η_w	dynamic viscosity of the wetting fluid	[$ML^{-1}T^{-1}$]
p_c	capillary pressure, Eq. (10)	[$ML^{-1}T^{-2}$]
U	capillary energy density, Eq. (9)	[$ML^{-1}T^{-2}$]
π_0	capillary modulus or reference pressure	[$ML^{-1}T^{-2}$]
m	van Genuchten model parameter (van Genuchten, 1980)	[–]
S_r^{res}	residual saturation degree of the wetting fluid	[–]
ρ_f	mass density of the non-uniform fluid, Eq. (3)	[ML^{-3}]
m_f	Lagrangian mass content of the non-uniform fluid	[ML^{-3}]
S_r	phase field parameter (or) order-parameter	[–]
$(.)'$	derivative w.r.t S_r	[–]
γ	surface tension between the two fluids that compose the non-uniform fluid	[MT^{-2}]
R	characteristic size of the pore throats that allows room for the non-uniform fluid	[L]
C	dimensionless parameter signifying the intensity of local bulk fluid energy w.r.t that of the capillary energy	[–]
C_k	coefficient of the non-local fluid energy	[MLT^{-2}]
μ_{pf}	chemical potential of the non-uniform pore fluid, Eq. (20)	[$ML^{-1}T^{-2}$]
μ_e	effective chemical potential of the non-uniform pore fluid, Eq. (22)	[$ML^{-1}T^{-2}$]
P	imposed linear pressure distribution	[$ML^{-1}T^{-2}$]
λ	gradient of the imposed linear pressure distribution	[$ML^{-2}T^{-2}$]
μ	augmented chemical potential w/ the imposed linear pressure contribution, Eq. (24)	[$ML^{-1}T^{-2}$]
c	characteristic speed of shock wave solutions, Eq. (34)	[–]
ξ	transformed coordinate w.r.t x	[–]
S_-, S_+	boundary conditions on the left and right respectively of a jump initial condition	[–],[–]
L	physical length of the one-dimensional domain used in numerical simulations	[L]
$\Delta x, \Delta t$	dimensionless spatial and temporal discretization sizes used for numerical resolution	[–],[–]
V_f	dimensionless injection velocity applied on a part of the boundary, Eq. (42) in numerical simulations	[–]
S_r^0, μ^0	initial saturation degree and dimensionless chemical potential used for resolving the spatio-temporal evolution in numerical simulations	[–],[–]
S_a, S_b	saturation degrees of the uniform intermediate states during the spatio-temporal evolution	[–],[–]
s, s_-, s_+	saturation degree, left and right boundary conditions in the moving coordinate system	[–],[–],[–]
$(s_e, 0, 0)$	equilibrium state associated to the dynamical system Eq. (49)	([–],[–],[–])

prescribed pressure difference between the two fluids, $(p_{nw} - p_w) = p_c(S_w)$, within a porous skeleton and so, is called the retention relation or the retention curve. In this sense, it accounts not only for the surface tension between the two fluids but also for the retention effect provided by the pore walls due their texture.

The thermodynamic consistency of this approach is further corroborated by the concept of energy separation (Coussy, 2004), wherein the bulk fluid energy density is considered apart from that of the interfaces and the overall interfacial energy density ($\phi\, U(S_w)$) is a priori accounted for in the free energy density of the porous solid,

$$\widehat{\Psi}_s = \psi_s + \phi\, U(S_w), \tag{1}$$

where the Lagrangian porosity of the skeleton, ϕ, is the ratio of porous volume in the current configuration to the total volume of the porous medium in the reference configuration. $\widehat{\Psi}_s$ and ψ_s are respectively, the free energy density of the porous solid in the classical approach and the free energy density of the porous skeleton. Such an approach allows to model ψ_s as a state function accounting for the tensile effect on the pore walls due to the presence of interfaces.

The functional form of $p_c(S_w)$ usually is empirical (van Genuchten, 1980; Brooks and Corey, 1964) in order to fit the experimental data and can generally be hysteretic. It has been noted over the years that such one-to-one relation between capillary pressure and saturation degree is not enough to describe non-local phenomena such as pinching and coalescence of fluids due to variations in capillary forces. Nevertheless, such a treatment is still widely in use.

Typically in soil hydrology, see Hilfer and Steinle (2014) for instance, water is considered to be in-compressible and its density, ρ_w, is assumed to be much higher compared to that of air, ρ_{nw}. Further the air phase is assumed continuously connected to the atmosphere leading to pressure gradients within that phase vanishing instantaneously. Consequently, the only relevant variables are those of the water phase: ρ_w, S_w and p_w. Such assumptions lead to the Richards equation,

$$\frac{\partial(\phi S_w)}{\partial t} + \nabla\cdot\left[\frac{\varkappa}{\eta_w}K_w(S_w)\Big(\nabla p_c(S_w) + \rho_w g e_x\Big)\right] = 0, \tag{2}$$

that governs the spatio-temporal evolution of the volume content of wetting fluid (ϕS_w). Here the acceleration due to gravity is assumed to be acting along the unit vector, e_x, in the x-direction. The fluid flow encompassed within the Richards equation is described by the extension of Darcy flow to the unsaturated conditions, the Darcy–Buckingham equation (Buckingham, 1907). $K_w(S_w)$ is thus a dimensionless relative permeability function which is a non-linear and typically empirical relation that modulates the flow of wetting fluid with respect to its saturation degree, increasing with S_w from 0 to 1.

In terms of stability, the works of Egorov et al. (2003), Nieber et al. (2005) revealed that the Richards equations is unconditionally stable against traversal perturbations thus being unable to produce experimentally observed fingering type instabilities. While various extensions have been proposed intending to remedy these inadequacies, we mention here a few of them. Hassanizadeh and Gray (1990), Gray and Hassanizadeh (1991) introduced the specific interfacial area, a

measure of the fluid interfaces, as an internal state variable thus providing a corrective term to an otherwise coarsely defined retention relation, $p_c(S_w)$. As part of their 'hold-back-pile-up' postulate Eliassi and Glass (2002) drew parallels to this corrective term, introducing the so-called 'hypo-diffusive' term and showed (Eliassi and Glass, 2003) that if this correction results in a non-monotonic retention relation then non-monotonic overshoot saturation profiles are possible in gravity driven infiltration. Eliassi and Glass (2002) also introduced a mixed 'relaxation' term, which is second order in space and first order in time, as an extension to standard Richards equation and interpreted this as a consequence of the rate-dependent capillary pressure function introduced by Majid Hassanizadeh and Gray (1993). Egorov et al. (2003), Nieber et al. (2005) have shown that such an extension to the Richards equation can produce instabilities for non-monotonic solution profiles. DiCarlo et al. (2008) used this relaxation term to introduce regularization to the Richards equation with non-monotonic capillary pressure function from Eliassi and Glass (2003) and showed similar overshoot solutions. Cueto-Felgueroso and Juanes (2009a) introduced in their model a fourth order in space term as an extension to the standard Richards equation producing non-monotonic solution profiles and proposed a relevant heuristic scaling of the fourth order coefficient that resulted in favorable comparison with some experimental observations. Stability analysis (Cueto-Felgueroso and Juanes, 2009b) of this model as well has revealed instabilities when saturation profiles are non-monotonic.

2.2. Phase field approach

More recently in the work of one of the authors (Sciarra, 2016), a framework has been built that is thermodynamically consistent and naturally allows for modeling possible localized deformations of the porous skeleton (Vardoulakis et al., 1978; Andò et al., 2012; Desrues and Andò, 2015) and its coupling to the fluid flow. Concerning the fluid description, while the standard retention curve describes the confining effect due to the pore walls, an enhanced description of surface tension between the fluids is obtained by considering the two immiscible fluids as a single non-uniform biphasic fluid in the spirit of Cahn and Hilliard (1958, 1959). In this sense it can be viewed as a phase field approach to model multi-phase fluid flow while accounting for the fact that the pore network, through which the non-uniform fluid is flowing, provides additional interfacial energy due to the solid–fluid interfaces. Such a description of fluids is adopted in the current study. Naturally within such a framework, coexistence of isopotential phases is possible thanks to the Van der Waals-like double-well form of the fluid energy density. This gives rise to a non-monotonic effective retention curve when the confining effect given by the standard retention curve is added to it. Parallels may be drawn to the 'hypo-diffusive' term (Eliassi and Glass, 2002; DiCarlo et al., 2008) which resulted in a non-monotonic retention relation, but the mixed 'relaxation' term is not employed in the current model. Instead, as usual in Cahn–Hilliard type phase field models (Lowengrub and Truskinovsky, 1998; Jacqmin, 2000; Boyer and Lapuerta, 2006; Kim, 2012), coarsening of the fluid domains and pattern formation is made possible due to a non-local gradient energy contribution giving rise to an extension to the Richards equation which is now fourth order in space. In this sense parallels may be as well drawn to the higher order model introduced by Cueto-Felgueroso and Juanes (2009a), which, however, does not account for coexistence of isopotential phases and phase segregation due to its lack of a bulk energy contribution that has a double-well structure.

2.2.1. Balance of mass

According to this adopted framework (Sciarra, 2016) the mixture of two immiscible fluids saturating the porous space is viewed as a single non-uniform biphasic fluid occupying the full porous space. This non-uniform fluid (further sub-scripted 'f') is furnished with an phase field/order parameter, S_r, in the spirit of Cahn–Hilliard modeling, which is an intensive scalar property distinguishing the two phases. The role of phase field parameter is chosen to be played by the classical Saturation degree of wetting fluid, S_w. This puts a physically motivated restriction on the range of values this phase field parameter can take, as such $S_r \in [0,1]$. $S_r = 0$ represents pure phase of air(non-wetting fluid) and $S_r = 1$ represents that of water(wetting fluid). This allows to invoke the assumptions (Hilfer and Steinle, 2014) that lead to Richards equation. For an $S_r \in [0,1]$, a simple linear interpolation of individual densities of pure phases can be assumed for the apparent density, ρ_f, of the non-uniform fluid (Kim, 2012). A non-uniform fluid composed of in-compressible water ($\rho_w = const$) and highly rarefied air, the latter being continuously connected to the atmosphere, implies that pure air phase is of infinite mobility. Thus any pressure differences in this phase ($S_r = 0$) are instantaneously vanishing and the pressure itself equates to that of reference atmospheric pressure, assumed 0 for convenience. Concurrently invoking an ideal gas law for air implies that its density, ρ_{nw}, is negligible compared to that of water ($\rho_w \gg \rho_{nw} \approx 0$) leading to,

$$\rho_f = \rho_w S_r + \rho_{nw}(1 - S_r) \approx \rho_w S_r. \tag{3}$$

This leads to a further simplification of the Lagrangian mass content of the non-uniform fluid per unit volume of the porous medium, $m_f = \rho_f \phi \approx \rho_w S_r \phi$. Following Coussy (2004), the local form of the overall balance of mass of the non-uniform fluid can be written as,

$$\rho_w \frac{\partial(\phi S_r)}{\partial t} + \nabla \cdot \boldsymbol{M} = 0. \tag{4}$$

In the above $\boldsymbol{M}$ [$\mathrm{ML^{-2}T^{-1}}$] is the Lagrangian fluid mass flow vector relative to the skeleton. While we lay down in brief the thermodynamic restrictions that lead to the possible constitutive prescriptions for $\boldsymbol{M}$, we refer the reader to Sciarra (2016) for a detailed treatment.

2.2.2. Fluid and interfacial energies

Since the model is based on the classical approach to poromechanics (Coussy, 2004, 2010), starting from the first and second principles of thermodynamics a free energy density of the porous solid, Ψ_s, is deduced subtracting the bulk contribution of the fluid, ($\phi\ \Psi_L$), from that of the overall porous medium,

$$\Psi_s = \Psi - \phi\ \Psi_L. \tag{5}$$

This approach has its origins in the work Biot (1972), according to which the porous solid is understood as a 'wetted' porous skeleton, with a thin layer of fluid attached to the pore walls, thus accounting for the associated interfaces. This allows one to model Ψ_s as a state function in the context of thermo-poroelasticity where dissipation is only attributed to the fluid flow and thermal effects.

Now, the main difference between the classical and the current phase field approaches lies in the prescription of the interfacial energies and the ensuing concept of energy separation. We start the following developments with the former. In the phase field approach, the fluid–fluid interfaces are considered apart from those of the solid–fluid interfaces. This is quite natural since a non-uniform fluid, in the sense of Cahn–Hilliard modeling, already accounts for any interfaces forming between its constituent phases, in this case air and water. At an ideal contact between two such immiscible fluids the interface is sharp and an associated jump, say in the phase field parameter, should exist. In a Cahn–Hilliard type modeling of multi-phase fluids (Lowengrub and Truskinovsky, 1998; Jacqmin, 2000; Boyer and Lapuerta, 2006; Kim, 2012), the sharp interface is approximated by a diffused counterpart with a finite thickness, ℓ, across which large variations of the phase field parameter occur. In this sense the current model intends to provide a smeared description of partial saturation and does not identify the position of pore-scale menisci that form within the network. An estimate of this intrinsic length, ℓ, can be obtained from physical measurements of transition lengths along the macroscopic air–water interface. As usual in Landau and Cahn–Hilliard models, in order to be

able to describe pattern formation during phase separation of the binary mixture, the free energy of the non-uniform fluid is defined as sum of a double-well potential, having isopotential minima in the pure phases, and a non-local gradient contribution. Thus for a given unit volume of porous medium in its reference configuration the free energy density of non-uniform fluid saturating its pores is as follows:

$$\phi\, \Psi_f(S_r, \nabla(\phi S_r)) = \phi\, \Psi_L(S_r) + \Psi_{NL}(\nabla(\phi S_r)), \tag{6}$$

where $\Psi_L(S_r)$, the local bulk contribution to the free energy as introduced in Eq. (5), is responsible for segregation and allows for coexistence of the immiscible phases. A possible form allowing for such description is

$$\Psi_L(S_r) = \frac{C\gamma}{R} S_r^2 \left(1 - S_r\right)^2, \tag{7}$$

which has a symmetric double-well structure whose isopotential minima correspond to pure phases of air ($S_r = 0$) and water ($S_r = 1$). See Fig. 1. The characteristic radius of channels within which the fluid menisci form, R, is an intrinsic property of the porous skeleton and according to Leverett (1941) it scales with $\sqrt{\varkappa/\phi_0}$. The derivative of $\Psi_L(S_r)$ w.r.t S_r gives a chemical potential, $\mu_L(S_r)$, whose negative spatial gradient is the local "force" that drives the distribution of the phases at equilibrium.

$\Psi_{NL}(\nabla(\phi S_r))$ is the non-local gradient contribution allowing the formation of diffuse interface between the two phases and provides regularization of the non-convex local energy. This term is assumed to be quadratic in gradient of fluid content, $\nabla(\phi S_r)$, as follows:

$$\Psi_{NL}(\nabla(\phi S_r)) = \frac{C_k}{2} \left((\nabla(\phi S_r)) \cdot (\nabla(\phi S_r))\right), \tag{8}$$

thus accounting not only for saturation gradients but also for gradients of porosity. The magnitude of C_k determines spatial influence of this non-local energy. The significance and choice of scaling of this term is reserved for later analysis. However, in case of a homogeneous evolution of S_r this term vanishes.

On the other hand, the classical capillary energy density, introduced in Eq. (1), now a function of the phase field parameter, $U(S_r)$, is assumed for the contribution of the solid–fluid interfaces, thus accounting for retention properties of the solid skeleton due to the texture of its pore walls. In the current study the widely used van Genuchten form (van Genuchten, 1980),

$$U(S_r) = \int_{S_r}^{1} p_c(S) dS, \tag{9}$$

$$p_c(S_r) = -\frac{\partial U}{\partial S_r} = \pi_0 \left(\left(\frac{S_r - S_r^{res}}{1 - S_r^{res}} \right)^{-\frac{1}{m}} - 1 \right)^{1-m}, \tag{10}$$

is assumed where, π_0 scales as $\rho_w g \ell_c$. ℓ_c [L] is the porous media counterpart of capillary length scale that relates intensity of capillary forces in the porous medium to that of gravity.

With such a description of interfacial energy contributions, the classical energy separation, Eq. (1) is revised to account for the non-local fluid energy contribution,

$$\Psi_s = \psi_s + \phi\, U(S_r) + \Psi_{NL}(\nabla(\phi S_r)). \tag{11}$$

In this sense, Eq. (5) now implies that the so-called porous solid comprises of the skeleton with a thin layer of fluid attached to the pore walls and as well all the fluid–fluid interfaces that form within the pore spaces. Thus, using Eq. (5) the overall free energy density of the porous medium can be written as,

$$\Psi = \psi_s + \phi\, \Psi_L(S_r) + \phi\, U(S_r) + \Psi_{NL}(\nabla(\phi S_r)). \tag{12}$$

If we consider a rigid porous skeleton ($\phi = \phi_0 = const$), as done further, then $\psi_s = 0$ and the contribution of the porous solid, Ψ_s, to the overall free energy of the porous medium reduces to just that of the interfaces resulting in,

$$\Psi = \phi\, \Psi_L(S_r) + \phi\, U(S_r) + \Psi_{NL}(\nabla(\phi S_r)). \tag{13}$$

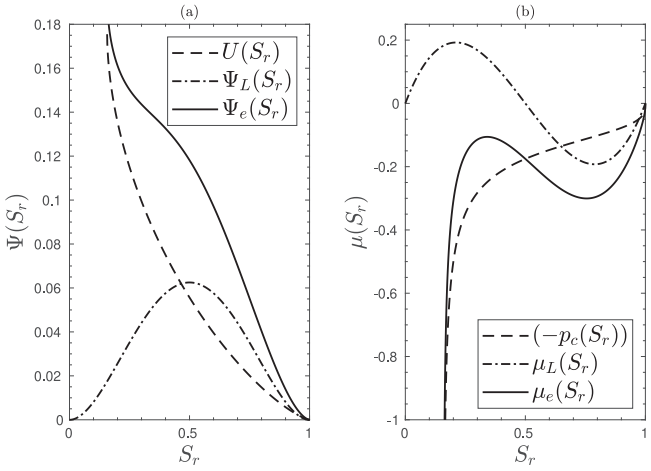

Fig. 1. (a) Energy densities, $\Psi_e(S_r)$, $\Psi_L(S_r)$, $U(S_r)$; (b) chemical potentials, $\mu_e(S_r)$, $\mu_L(S_r)$, $p_c(S_r)$. All functions plotted are dimensionless according to the scheme presented in Section 2.2.7.

2.2.3. Dissipation and generalized Darcy's law

In what follows the main implications of dissipation inequality in the framework of above mentioned modeling scheme are reported. Interested reader may find a formal deduction of them in Sciarra (2016). Also, it is to be noted that the Cahn–Hilliard nature of the fluid energy should imply that a suitable entropy function can be defined similar to what was done in Beljadid et al. (2020) and an underlying gradient flow structure can be identified (Cancès et al., 2019). However, this is beyond the scope of the current work.

Starting from the fluid mass balance, the principles of thermodynamics and the constitutive prescription of the non-uniform fluid, a characterization of dissipation of the overall porous medium can be obtained. The primary assumption of a rigid porous skeleton a priori allows one to neglect the power of external forces acting to deform the skeleton itself and consequently any power of internal forces acting to generate solid strains. So, any dissipative phenomena should be restricted to the fluid flow, interfacial changes and thermal effects. Referring to the developments in Sciarra (2016) and those presented above, the overall dissipation of the porous medium, Φ, is given in the form of a Clausius–Duhem inequality,

$$\Phi = \Phi_s + \Phi_f + \Phi_{th} \geq 0, \tag{14}$$

where Φ_s, Φ_f, and Φ_{th} are the dissipations related respectively to the solid skeleton, non-uniform fluid flow and thermal effects, whose particular expressions are given below. As a general practice in poromechanics (Coussy, 2004), these three contributions are independently assumed non-negative in order to satisfy Eq. (14) so that,

$$\Phi_s = \phi \frac{\partial U}{\partial S_r} \frac{dS_r}{dt} + \frac{\partial \Psi_{NL}}{\partial(\nabla(\phi S_r))} \cdot \frac{d(\nabla(\phi S_r))}{dt} - S_s \frac{dT}{dt} - \frac{d\Psi_s}{dt} \geq 0, \tag{15}$$

$$\Phi_f = -\left\{ \nabla \left[\frac{\partial \Psi_L}{\partial S_r} + \frac{\partial U}{\partial S_r} - \nabla \cdot \left(\frac{\partial \Psi_{NL}}{\partial(\nabla(\phi S_r))} \right) \right] - \frac{\mathfrak{b}_f}{\phi S_r} \right\} \cdot \frac{M}{\rho_w} \geq 0, \tag{16}$$

$$\Phi_{th} = -\frac{\mathfrak{q}}{T} \cdot \nabla T \geq 0, \tag{17}$$

where $\mathfrak{b}_f$ [$ML^{-2}T^{-2}$] is the bulk force acting on the fluid, $\mathfrak{q}$ [MT^{-3}] is the surface heat flux vector, T [Θ] is the absolute temperature and S_s [$ML^{-1}T^{-2}\Theta^{-1}$] is the entropy density of the porous solid. Eq. (15) states that in the context of thermo-poroelasticity, if the skeleton is assumed to be rigid then the free energy of the skeleton must still account for the interfacial phenomenon due to variations in saturation degree and its spatial gradient. In other words, under isothermal conditions, $\Psi_s(S_r, \nabla(\phi S_r))$ is a state function which in the current framework is given by Eq. (11) with $\psi_s = 0$. Eq. (17) states that heat flows from regions of higher temperature to those of lower temperature along the direction of negative gradient of the temperature. Under isothermal conditions, as considered further, this dissipative contribution is vanishing.

The dissipation due to fluid flow is encompassed within Eq. (16). In essence the generalized force, coefficient of (M/ρ_w), causing the fluid flow must be related to the fluid velocity vector in such a way as to satisfy the dissipation inequality. One way to achieve this, which is an usual practice in poromechanics, is to assume a linear relationship with a coefficient of proportionality that could depend on the intrinsic permeability of the skeleton, saturation degree and dynamic viscosity of the fluid,

$$\begin{aligned} M &= \rho_w V \\ &= \rho_w \frac{\varkappa}{\eta_w} K(S_r) \left\{ -\nabla \left[\frac{\partial \Psi_L}{\partial S_r} + \frac{\partial U}{\partial S_r} - \nabla \cdot \left(\frac{\partial \Psi_{NL}}{\partial(\nabla(\phi S_r))} \right) \right] \right. \\ &\quad \left. + \frac{\mathfrak{b}_f}{\phi S_r} \right\}, \end{aligned} \tag{18}$$

where V [LT^{-1}] is the fluid velocity vector. This approach is equivalent to the extension of Darcy's law to unsaturated flow conditions. $K(S_r)$ is a dimensionless function that accounts for the non-uniform resistance to the flow experienced by the fluid due to its non-uniform nature. Accordingly in the pure air phase ($S_r = 0$) the non-uniform fluid must be infinitely mobile, $K(S_r) = 0$. And when the pore network is fully saturated by water ($S_r = 1$), one should recover the Darcy-like relation in full saturation with $K(S_r) = 1$. In this way Eq. (18) is a generalized form of the Darcy's law and the classical counterpart of $K(S_r)$ is the relative permeability $K_w(S_w)$ introduced in Eq. (2). It is to be noted that, in Eq. (18) an isotropy of the flow within the porous medium has been assumed. Eq. (18) and (16) imply that the fluid dissipation now reads,

$$\Phi_f = \frac{\eta_w}{\varkappa\, K(S_r)} \frac{(M \cdot M)}{\rho_w^2} \geq 0. \tag{19}$$

This results in a restriction on the function $K(S_r)$ to be positive in order to ensure the positiveness of the dissipation associated to the fluid flow. Moreover, it is worth to note at this point that there is no restriction due to thermodynamic principles on the convexity of the function $K(S_r)$. The particular form employed for this function in the current work is motivated further in Section 3.

2.2.4. Towards a non-uniform pore fluid

Looking at Eq. (18), in the absence of a bulk force acting on the fluid, $\mathfrak{b}_f = 0$, the generalized force driving the flow is the negative spatial gradient of a chemical potential identified as,

$$\mu_{pf} = \frac{\partial \Psi_L}{\partial S_r} + \frac{\partial U}{\partial S_r} - \nabla \cdot \left(\frac{\partial \Psi_{NL}}{\partial(\nabla(\phi S_r))} \right), \tag{20}$$

where a new sub-script 'pf' is introduced that represents a supposed 'non-uniform pore fluid' that is understood as a non-uniform fluid, as introduced in Section 2.2.2, that is confined within a pore network characterized by the capillary energy $U(S_r)$. As usual in Cahn–Hilliard type modeling, this chemical potential, μ_{pf}, can be derived as a variational derivative w.r.t to S_r of an overall free energy of the non-uniform pore fluid. The density of such an overall free energy, Ψ_{pf}, in the current case can clearly be identified by the overall free energy density of the porous medium, Ψ, with a rigid porous skeleton given by Eq. (13),

$$\Psi_{pf} = \Psi = \phi\, \Psi_L(S_r) + \phi\, U(S_r) + \Psi_{NL}(\nabla(\phi S_r)). \tag{21}$$

It is worth noting that unlike $\Psi_L(S_r)$, the local part of this new energy density, $(\Psi_L(S_r) + U(S_r))$, has no more a symmetric double-well structure between $S_r = 0$ and 1. Instead, the minimum associated to $S_r = 0$ no more exists and only one global minimum remains at $S_r = 1$. See Fig. 1. Moreover, depending on the relative intensities of bulk and capillary energy densities it is possible also that a minimum associated to lower S_r exists, but is shifted inwards of the original range of S_r thus changing the corresponding local preferential states at equilibrium (Sciarra, 2016). However, these two minima would not be isopotential. In both these cases, when the chemical potential is non-monotonic, Maxwell construction (equal-area rule) can be understood as a search for the line bi-tangent to this new energy density at equilibrium conditions of the non-uniform pore fluid. This is equivalent to construction of a linear potential due to external forces which once accounted for brings back the double-well structure with two isopotential minima. Now these two minima, both shifted inwards of original range of S_r, being isopotential allows for coexistence between the corresponding phases. The inward shift of the minima can be understood as a correction to account for wetting properties of the skeleton at equilibrium in the case of lower minimum and as a correction to account for trapped air in the case of higher minimum shifted from $S_r = 1$. Owing to this significance of physical interpretation, this local contribution in Eq. (21) is further referred to as the effective energy density, $\Psi_e(S_r) = \Psi_L(S_r) + U(S_r)$, of the non-uniform pore fluid and its partial derivative w.r.t S_r, the effective chemical potential, see Fig. 1,

$$\mu_e(S_r) = \frac{\partial \Psi_L}{\partial S_r} + \frac{\partial U}{\partial S_r} = \mu_L(S_r) - p_c(S_r). \tag{22}$$

2.2.5. Phase field governing equation

With the above framework established, one can obtain the spatio-temporal evolution of S_r and M by resolving the coupled system of partial differential equations (PDEs) formed by the balance of mass, Eq. (4), and the generalized Darcy's law, Eq. (18). An alternative way, which renders the equations amenable for the current analysis is to resolve, for the evolution of S_r, a fourth order PDE formed by substituting Eq. (18) into Eq. (4),

$$\phi \frac{\partial S_r}{\partial t} + \nabla \cdot \left[\frac{\varkappa}{\eta_w} K(S_r) \left(-\nabla \mu_{pf} + \frac{\mathfrak{b}_f}{\phi S_r} \right) \right] = 0. \tag{23}$$

In the above, the expression of $\mu_{pf}(S_r, \nabla S_r)$ is given by Eq. (20) and $\phi = \phi_0 = const$ in accordance with the assumption of a rigid porous skeleton. In soil hydrology and various other practical applications like CO_2 sequestration, the bulk force acting on the fluid is due to gravity. If we consider gravitational acceleration to be acting in the positive x-direction, then $\mathfrak{b}_f = m_f g e_x \approx \rho_w S_r \phi g e_x$ in accordance with Eq. (3). The structure of the above equation closely resembles that of the classical Richards equation, Eq. (2). The difference lies in the constitutive prescription that lead to the particular expression of $\mu_{pf}(S_r, \nabla S_r)$ in Eq. (23) compared to that of $p_c(S_w)$ in Eq. (2).

In what follows, a more general case is considered by introducing an additional linear pressure distribution which potentially allows to describe an initial uniform background mean flow. This state can then be perturbed by modifying the boundary conditions in order to investigate the evolution of either a drainage or an imbibition front. Thus an augmented chemical potential incorporating both the effects of initial background mean flow and of gravity forces is written as,

$$\mu = \mu_{pf} + P, \tag{24}$$

where the pressure distribution $P = -\lambda x$. In the case when only gravity forces are considered P is just proportional to $\lambda = \rho_w g$. Both these

scenarios may coexist in which case gravity can act to either stabilize or destabilize the motion of an air–water front depending on their relative directions.

2.2.6. Summary of the model - Governing equations

Introducing the above mentioned augmented chemical potential, μ, the governing equation for S_r, Eq. (23), can be re-written as follows,

$$\phi\frac{\partial S_r}{\partial t}+\frac{\varkappa\lambda}{\eta_w}\frac{\partial K(S_r)}{\partial x}-\frac{\varkappa}{\eta_w}\nabla\cdot\left[K(S_r)\left(\nabla\mu_{pf}\right)\right]=0, \tag{25}$$

with μ_{pf} given by Eq. (20) and reported again below for the sake of clarity,

$$\mu_{pf}=\frac{\partial\Psi_L}{\partial S_r}+\frac{\partial U}{\partial S_r}-\nabla\cdot\left(\frac{\partial\Psi_{NL}}{\partial(\nabla(\phi S_r))}\right).$$

The quantity $\varkappa\lambda/\eta_w$ [LT^{-1}] can be identified as the magnitude of a saturated mean velocity, V_m, in the porous medium. In essence this quantity represents the intensity of advection of non-uniform pore fluid, in other words that of the phase field parameter S_r. Appropriate boundary conditions will be introduced in Sections 3.1.1 and 3.1.2 to close the problem.

2.2.7. Dimensional analysis and scaling

The effective dimension of Eq. (25) is [T^{-1}]. To render the equation dimensionless the following dimensionless variables ($\tilde{\cdot}$) and corresponding characteristic scaling numbers (sub-scripted 'h') are introduced:

$$\tilde{x}=\frac{x}{x_h}\ ,\quad \tilde{\mu}_{pf}=\frac{\mu_{pf}}{p_h}=\frac{\mu_{pf}R}{C\gamma}\ ,\quad \tilde{t}=\frac{t}{t_h}=\frac{tV_m}{x_h}. \tag{26}$$

The time scale is chosen to make unity the coefficient in front of advection term, $t_h=x_h/V_m$. And a particular grouping of parameters results in the dimensionless equation,

$$\phi\frac{\partial S_r}{\partial\tilde{t}}+\frac{\partial K(S_r)}{\partial\tilde{x}}-\frac{\delta_R}{C_a}\tilde{\nabla}\cdot\left[K(S_r)\left(\tilde{\nabla}\tilde{\mu}_{pf}\right)\right]=0. \tag{27}$$

The dimensionless effective chemical potential of the non-uniform pore fluid, $\tilde{\mu}_{pf}$, along with the linear pressure contribution, $\tilde{P}$, can be written, employing the particular expressions introduced in Section 2.2.2, as,

$$\begin{aligned}\tilde{\mu}&=\tilde{\mu}_{pf}+\tilde{P}\\&=2S_r\left(1-3S_r+2S_r^2\right)-D_U\left(\left(\frac{S_r-S_r^{res}}{1-S_r^{res}}\right)^{-\frac{1}{m}}-1\right)^{1-m}\\&\quad-D_{NL}\tilde{\nabla}\cdot\left(\tilde{\nabla}(\phi S_r)\right)-\frac{C_a}{\delta_R}\tilde{x}.\end{aligned} \tag{28}$$

The dimensionless numbers C_a, δ_R, D_U and D_{NL} are identified as follows:

$$\begin{aligned}C_a&=\frac{V_m\eta_w R^2}{\varkappa C\gamma}\ ,\quad \delta_R=\frac{R}{x_h},\\D_U&=\frac{\pi_0 R}{C\gamma}\ ,\quad D_{NL}=\frac{C_k R}{C\gamma x_h^2}=\frac{\pi_k R}{C\gamma}\left(\frac{\ell}{x_h}\right)^2.\end{aligned} \tag{29}$$

Here, C_a is the Capillary number signifying the competition between viscous forces and capillary forces at the air–water interface. δ_R is the ratio of characteristic radius of porous channels to the reference length scale. D_U is a measure of relative strength of the coefficients of capillary interfacial energy and the air–water interfacial energy. And D_{NL} is the so-called Cahn number, signifying intensity of the gradient energy with respect to the diffusive term. Above in Eq. (29) it is shown that the expression of D_{NL} can be recast such that the interface thickness, ℓ, is introduced into the equations and a free parameter, π_k [$\mathrm{ML}^{-1}\mathrm{T}^{-2}$], appears. This allows an input to the model from experimental measurements of observed macroscopic transition lengths. Further in this work, the length scale, x_h, is chosen to be the characteristic physical length of the domain under consideration. These choices are shown further to produce transition lengths of order ℓ in the numerical solutions when flow is driven by gravity. The full dimensionless form using Eq. (28) in Eq. (27), with the above choices of dimensionless numbers is as follows,

$$\begin{aligned}\phi\frac{\partial S_r}{\partial t}+\frac{\partial K(S_r)}{\partial x}-\frac{\delta_R}{C_a}\nabla\cdot\Bigg[K(S_r)\Bigg(\nabla\Bigg[2S_r\left(1-3S_r+2S_r^2\right)\\-D_U\left(\left(\frac{S_r-S_r^{res}}{1-S_r^{res}}\right)^{-\frac{1}{m}}-1\right)^{1-m}\Bigg]-D_{NL}\nabla\Delta(\phi S_r)\Bigg)\Bigg]=0.\end{aligned} \tag{30}$$

It is to be noted that ($\tilde{\cdot}$) has been dropped in Eq. (30) and is done so further in this work. So, from this point all the variables are dimensionless unless either mentioned otherwise or referred to from earlier sections.

3. One-dimensional analysis

In the work of Saffman and Taylor (1958), a fundamental study of the stability of fluid–fluid interface has been done in an analogous Hele-Shaw flow context. In order to perform this, an horizontal sharp interface has been assumed to separate two fluids of different viscosities moving within a Hele-Shaw cell, under the forces of gravity and pressure gradient. Upon this horizontal interface, wave like disturbances of variable wavelengths have been assumed and their growth in time has been understood as the typical fingering instability. Furthermore, surface tension has been shown to introduce a lower bound for the range of wavelengths of disturbances for which the interface is unstable.

It is the intention of this current study to characterize within the framework of the adopted model, propagation of an air–water interface both in the case of imbibition and in drainage. And in the Part II the stability/instability of these interfaces will be investigated. Therefore, as a first step transversely homogeneous solutions of Eq. (30) that represent such interfaces need to be built.

In this section we observe that solutions assuming transverse homogeneity in y and z-directions but evolving longitudinally along x-coordinate, are composed of similarity solutions of the one-dimensional equation

$$\begin{aligned}\phi\frac{\partial S_r}{\partial t}+\frac{\partial K(S_r)}{\partial x}-\frac{\delta_R}{C_a}\frac{\partial}{\partial x}\left(K(S_r)\mu_e'(S_r)\frac{\partial S_r}{\partial x}\right)\\+\frac{\delta_R}{C_a}\phi D_{NL}\frac{\partial}{\partial x}\left(K(S_r)\frac{\partial^3 S_r}{\partial x^3}\right)=0.\end{aligned} \tag{31}$$

In the above, the definition of effective chemical potential of non-uniform pore fluid, $\mu_e(S_r)$ (Eq. (22)), is invoked.

At larger spatial scales compared to both the length scale of the air–water interface and that of diffusion, the solutions of Eq. (31) are regularized solutions of the corresponding scalar hyperbolic conservation law (LeFloch, 2002) in the limit of vanishing diffusion. Assuming such limit, Eq. (31) simplifies as

$$\phi\frac{\partial S_r}{\partial t}+\frac{\partial K(S_r)}{\partial x}=0. \tag{32}$$

Here, the function $K(S_r)$ plays the role of an advective flux. A class of weak solutions of a Riemann problem governed by Eq. (32), given a

Table 2
Material properties, model parameters used through Section 3, unless mentioned otherwise.

$\varkappa$ [m^2]	η_w [Pa s]	ϕ [−]	C [−]	γ [N m^{-1}]	R [m]	π_0 [Pa]	m [−]	S_r^{res} [−]	C_k [N]	ℓ [m]
1.0E−12	8.9E−04	0.37	0.5	0.073	1.64E−06	2840.91	0.685	0.1567	113.66	0.2

piece-wise uniform initial condition with a jump between S_- and S_+ at $x = 0$, that represent sharp displacement of one fluid by another, are piece-wise uniform functions known as shocks,

$$S_r(x,t) = \begin{cases} S_- & if \quad x < ct \\ S_+ & if \quad x > ct, \end{cases} \tag{33}$$

that move with a characteristic speed, c. These solutions are self-similar in nature with respect to the transformation $\xi = x - ct$ and propagate along the x-coordinate while satisfying the Rankine–Hugoniot jump condition,

$$K(S_+) - K(S_-) = c\phi(S_+ - S_-), \tag{34}$$

that relates the speed of the shock wave to the uniform solution values on either side of the shock. A shock is considered classical or 'compressive' if the characteristics on either side of the shock impinge onto it. This condition is given by the celebrated Lax Entropy condition, which in the current case can be written as

$$K'(S_+) \leqslant \phi c \leqslant K'(S_-). \tag{35}$$

Apart from shocks, the class of smooth monotone weak solutions of the Riemann problem governed by Eq. (32) are rarefaction waves connecting S_- to S_+. These solutions are expansive and self-similar with respect to the transformation $\xi = x/t$. These are described by the following form:

$$S_r(x,t) = \begin{cases} S_- & if \quad \phi x < t\ K'(S_-) \\ K'^{-1}(\phi x/t) & if \quad t\ K'(S_-) < \phi x < t\ K'(S_+) \\ S_+ & if \quad \phi x > t\ K'(S_+). \end{cases} \tag{36}$$

When the flux function, $K(S_r)$, is purely convex and increasing, the only possible weak solutions are either classical shocks (if $S_- > S_+$) or rarefaction waves (if $S_- < S_+$) and analogously for purely concave flux function (LeFloch, 2002). In the presence of diffusion these sharp classical shock solutions satisfying Eq. (35), tend to be smeared up to a finite distance. On the other hand, for flux functions that have inflection points the structure of solutions is much more rich in the presence of higher order diffusion/dispersion. For instance smeared shock solutions that violate Eq. (35) can exist, which are considered to be non-classical (Bertozzi et al., 1999; Hayes and Shearer, 1999). The class of non-classical shocks for which the characteristics on either side pass through the shock are termed 'under-compressive' (Dukler et al., 2020) and they satisfy either of

$$K'(S_\pm) \leqslant \phi c \ ; \quad K'(S_\pm) \geqslant \phi c. \tag{37}$$

And those for which the characteristics behind and in the front seem to expand the shock itself are termed 'expansion' shocks (El et al., 2016) and they violate Eq. (35) as

$$K'(S_-) \leqslant \phi c \leqslant K'(S_+). \tag{38}$$

Presence of these solutions and their manifestation as traveling waves in the solution structure of imbibition and drainage problems governed by Eq. (31) are shown in the following section. Further in Section 3.2, the traveling wave part of these solutions are resolved in a one-dimensional setting.

As mentioned earlier, the nature of the flux function, $K(S_r)$, has an important effect on the structure of solutions that represent air–water displacements. In classical partial saturation (Coussy, 2004), the role of modulating the individual fluid velocities in space accordingly to their respective saturation degree is played by the relative permeability function. In the current study we intend to use the functional form of such a relative permeability of water for the flux function, owing to the phase field parameter, S_r, of the current model being representative of the saturation degree of water.

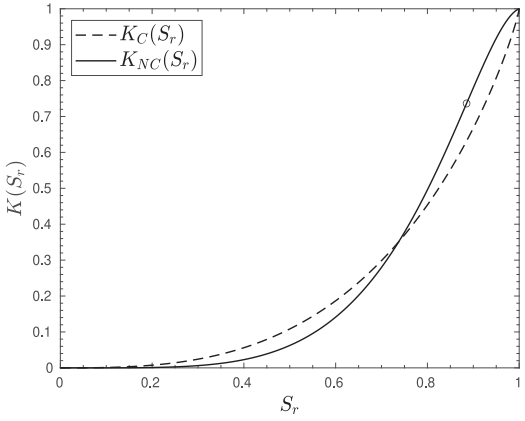

Fig. 2. Relative permeability functions $K(S_r)$, Eq. (39), for different values of van Genuchten parameters (a, b, c). K_C:(1.175, 0.85, 2.0), K_{NC}:(8.0, 2.0, 0.5). Inflection point is shown as a circle on curve $K_{NC}(S_r)$.

Typically unsaturated relative permeability functions used for various soils and fluid combinations are parametric models in order to fit experimental data. Especially in soil hydrology when fluid combination is water and wet air the well known van Genuchten model (van Genuchten, 1980; Luckner et al., 1989) is widely used which has the following form:

$$K(S_r) = \sqrt{S_r}\left[1 - \left(1 - {S_r}^a\right)^b\right]^c, \tag{39}$$

where a, b and c are real constants obtained through fitting with experimental results. As can be seen in Fig. 2, this functional form has the possibility to model a purely convex behavior, $K_C(S_r)$, and as well a convex–concave behavior, $K_{NC}(S_r)$. In what follows, in order to account for consolidation of the porous skeleton (Bear, 1972) and to demonstrate in the context of the current phase field model the possibility of modeling air–water displacements representing both imbibition and drainage, we employ the convex–concave function, $K(S_r) = K_{NC}(S_r)$, with $a = 8.0$, $b = 2.0$ and $c = 0.5$.

3.1. PDE simulations

In the current section we characterize the spatio-temporal evolution of solutions both in imbibition and drainage scenarios. To do this we choose the primary unknowns as the Saturation degree, S_r, and the regularized effective chemical potential with known spatially linear pressure contribution, μ. Then the coupled system of equations formed by Eqs. (27) and (28) is resolved. We acknowledge at this point that since our focus is to analyze the general structure and evolution of the solutions, we have adopted a simplest numerical discretization. One can definitely extend this to more sophisticated techniques of the likes of adaptive refinement (Martin et al., 2005; Boyer et al., 2009) and non-local operator methods (Ren et al., 2021).

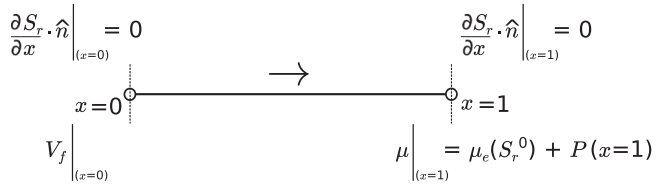

Fig. 3. Schematic of the imbibition simulations showing boundary conditions applied on the one-dimensional domain. The arrow indicates the direction of motion of the self-similar interface. The form of natural boundary condition $V_f(x=0)$ is given in Eq. (43).

Table 3
Dimensionless numbers corresponding to the material properties and model parameters in Table. 2 used through Section 3, unless mentioned otherwise.

C_a	δ_R	D_U	D_{NL}
7.4E−07	1.64E−08	0.128	5.12E−07

Spatial discretization is done employing a standard Galerkin formulation and linear Lagrange finite elements. Time discretization is done using the implicit Euler scheme of first order. The discrete solutions at nth time step, S_r^n and μ^n, are obtained by searching in the Hilbert space of admissible functions given by the cartesian product $\mathbb{H}_s \times \mathbb{H}_\mu$, with

$$\begin{aligned}\mathbb{H}_s &:= \left\{S_r^n \in H^1(\Omega) : S_r^n = \bar{S}_r^n \ on\ \partial\Omega_s\right\}\\ \mathbb{H}_\mu &:= \left\{\mu^n \in H^1(\Omega) : \mu^n = \bar{\mu}^n \ on\ \partial\Omega_\mu\right\}\end{aligned} \tag{40}$$

defined over the discretized domain Ω, so that the ordered couple (S_r^n, μ^n) solve the non-linear coupled variational system,

$$\begin{aligned}&\int_\Omega \hat{q}\left(\frac{\phi\left(S_r^n - S_r^{n-1}\right)}{\Delta t}\right)d\Omega + \int_\Omega \frac{\delta_R}{C_a}K(S_r^n)\left(\nabla\hat{q}\cdot\nabla\mu^n\right)d\Omega\\ &\qquad - \int_{\Omega_{N\mu}} \hat{q}\left(\frac{\delta_R}{C_a}K(S_r^n)\nabla\mu^n\right)\cdot\hat{n}\, d\Omega_{N\mu} = 0,\\ &\int_\Omega \hat{S}\left(\mu^n - \mu_e(S_r^n) + \frac{C_a}{\delta_R}x\right)d\Omega - \int_\Omega \phi D_{NL}\left(\nabla\hat{S}\cdot\nabla S_r^n\right)d\Omega\\ &\qquad + \int_{\Omega_{Ns}} \hat{S}\left(\phi D_{NL}\nabla S_r^n\right)\cdot\hat{n}\, d\Omega_{Ns} = 0.\end{aligned} \tag{41}$$

Here $\hat{q}$ and $\hat{S}$ are test functions belonging to the Hilbert space $(\mathbb{H}_s)_0 \times (\mathbb{H}_\mu)_0$ of functions which vanish on $\partial\Omega_s$ and $\partial\Omega_\mu$ where the values of S_r and μ are specified respectively. $\hat{n}$ is the outward unit normal vector to the boundary where it is referred to. $\Omega_{N\mu}$ is the part of the boundary where normal derivative of μ is specified, which translates to imposing at that part of the boundary an injection or extraction velocity of the fluid with a natural form,

$$V_f = -\frac{\delta_R}{C_a}K(S_r)\nabla\mu. \tag{42}$$

Ω_{Ns} is part of the boundary where normal derivative of S_r is specified. For one-dimensional simulations the computational domain is chosen along the positive x-direction such that $x \in [0,1]$. The corresponding physical length, $L = 100$m, is chosen to be sufficiently large such that the limit of vanishing diffusion as discussed earlier is valid. The material properties of the porous medium and the parameters of the model chosen for the purpose of demonstration are listed in Table 2, which are in the range typical of silica sands saturated with air–water mixture. The corresponding dimensionless numbers defined in Section 2.2.7 are listed in Table 3.

Mesh convergence behavior has been tested, once chosen initial and boundary conditions corresponding to an imbibition and a drainage problem, which are elaborated in Sections 3.1.1 and 3.1.2, to validate the numerical solution. In particular successively refined discretization steps have been considered. The results of this analysis are reported in Appendix B.

3.1.1. Imbibition

Displacement of air by water representing imbibition can be understood as a solution which transitions from a higher degree of saturation to a lower one and moves in the direction of the lower saturation. According to characteristic water retention properties of the porous skeleton, see Table 2, the appropriate initial condition for imbibition is set to $S_r^0 = 0.20$ throughout the domain, which is close to the residual saturation, S_r^{res}, and $\mu^0 = \mu_{pf}(S_r^0) + P$. For all $t > 0$, the normal derivative of S_r is set to vanish at both the boundaries, $x = 0$ and $x = 1$. See schematic Fig. 3. At the left boundary an injection velocity,

$$V_f\Big|_{(x=0)} = -\frac{\delta_R}{C_a}K(S_-)\nabla P, \tag{43}$$

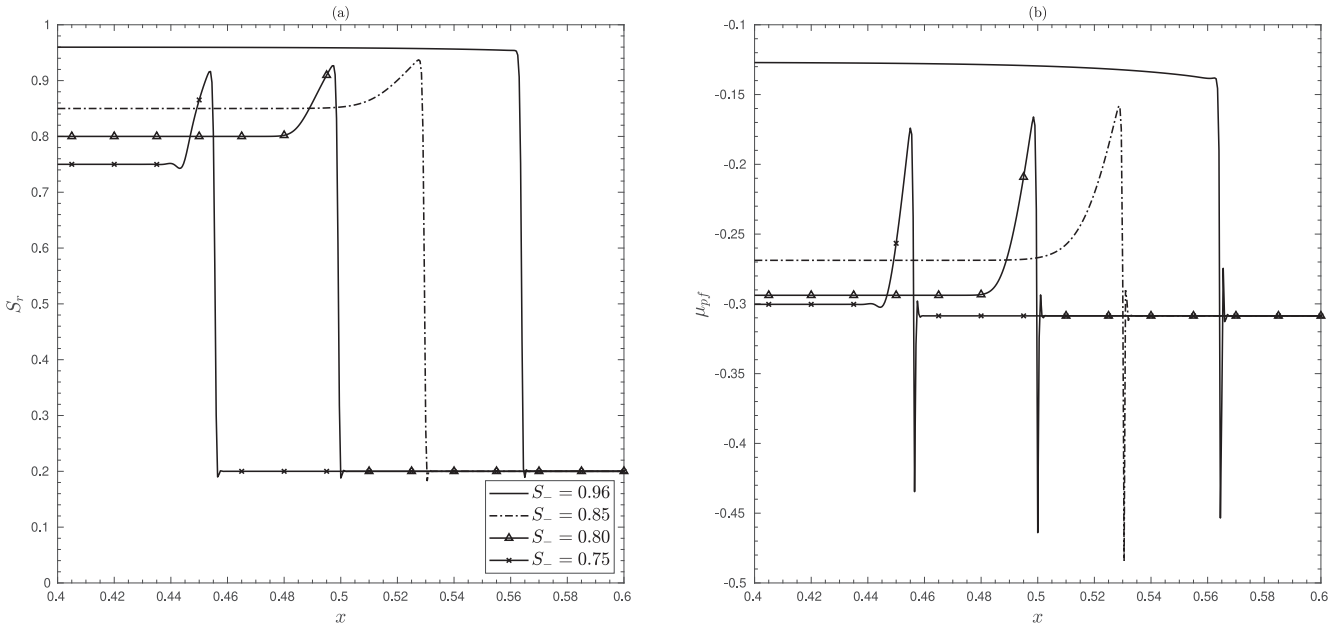

Fig. 4. One dimensional imbibition solutions of the coupled system Eq. (41), for $\lambda = \rho_w g$, with initial condition $S_r^0 = 0.20$ and boundary conditions corresponding to a constant rate of injection Eq. (43) with $S_- = 0.96, 0.85, 0.80, 0.75$, Δt = 1E-05, Δx = 5E-04, (a) Saturation degree, S_r, (b) regularized effective chemical potential, μ_{pf}. Solutions are shown at different time-steps and restricted spatial range for clarity. Out of this range, solutions are continuous and uniform extensions up to their respective boundary conditions.

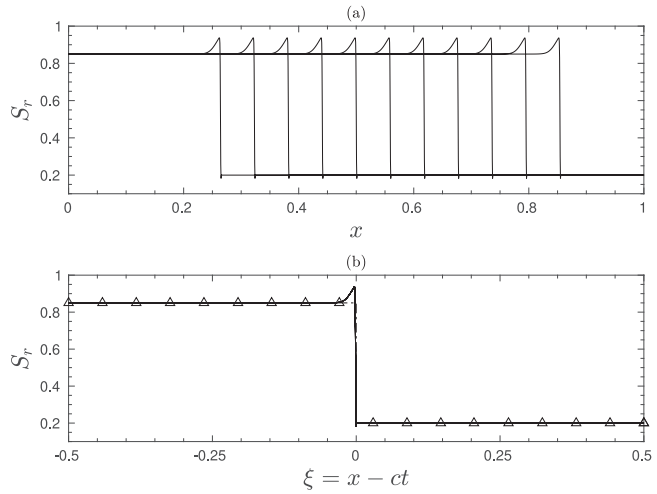

Fig. 5. One dimensional imbibition solution S_r of the coupled system Eq. (41), for $\lambda = \rho_w g$, $S_r^0 = 0.20$ and $S_- = 0.85$; (a) Solution at various time steps, (b) Solutions in (a) transformed into the TW-coordinate $\xi = x - ct$ with $c \approx 2.63$ given by Eq. (34). Shock solution, Eq. (33), for $S_- = 0.85$ and $S_+ = S_r^0 = 0.20$ is shown with triangle markers.

is imposed. This has an effect of perturbing the saturation degree at the left boundary towards $S_- > S_r^0$, inducing imbibition, while the normal derivative of μ_{pf} vanishes. The boundary at the right, $x = 1$, is drained with a Dirichlet boundary condition on μ such that,

$$\mu\Big|_{(x=1)} = \mu_e(S_r^0) + P(x = 1). \tag{44}$$

The results of simulations for various values of S_- and $\lambda = \rho_w g$ are shown in Fig. 4. The diffused interface in the solution connecting a higher value of S_r to a lower value represents the infiltration of water into a fluid-poor domain under the presence of gravity acting in the positive x-direction. The profile within the domain, of the regularized effective chemical potential, μ_{pf}, follows that of the S_r solution according to Eq. (20), with a strong gradient effect due to the interface. While all the saturation profiles are non-monotonic in the vicinity of S_r^0, there exist overshoot and non-overshoot behaviors behind the invading front. The reasoning for presence or absence of such overshoots and the oscillatory behavior around S_r^0 is reserved for analysis in the further sections.

However, in all these solutions the transition from S_- to S_r^0 seems to translate self-similarly in space suggesting the presence of traveling wave type higher order approximations of shock solutions. This observation is justified by a transformation into a TW-coordinate, $\xi = x - ct$, where c is given by Eq. (34) with $S_+ = S_r^0$, see Fig. 5. This results in the transition region of the solution to collapse into the vicinity of a single location, $\xi = 0$. The self-similar shock solution, Eq. (33), of the hyperbolic equation, Eq. (32), as well is plotted in the same TW-coordinate in Fig. 5. In Section 3.2.1 these TW-solutions are resolved and are shown to be classical or compressive in the sense of shocks.

3.1.2. Drainage

Drainage of water by air is understood as the contrary of imbibition, which is a transition from lower saturation degree to higher, moving in the direction of the higher saturation. So the initial condition is chosen as $S_r^0 = 0.99$ which is close to fully saturated condition, and $\mu^0 = \mu_{pf}(S_r^0) + P$. Owing to the phase field parameter, S_r, of the current model being representative of the saturation degree of water, an injection flux of the form Eq. (42) at the boundary would not be appropriate to induce drainage. Instead the initial condition is perturbed at the left boundary, $x = 0$, by imposing gradually decreasing Dirichlet boundary conditions on S_r and μ until the intended air saturation, S_r^d and $\mu^d = \mu_e(S_r^d)$ are achieved within a finite time, t_d, and then those

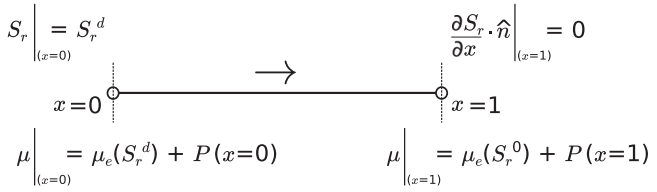

Fig. 6. Schematic of the drainage simulations showing boundary conditions applied on the one-dimensional domain for $t > t_d$. The arrow indicates the direction of motion of the self-similar interface.

boundary conditions are kept constant for all $t > t_d$. See schematic Fig. 6. The boundary at $x = 1$ is drained with a Dirichlet boundary condition on μ, Eq. (44), and the normal derivative of S_r is set to vanish for all $t > 0$ similar to the imbibition case.

Fig. 7 shows the solutions for various values of S_r^d and $\lambda = \rho_w g$. We note that the solution at later times is composed of an expanding part connecting S_r^d to an uniform state, S_b, which is then connected by a sharper transition to another uniform state S_a. S_a then connects to S_r^0 through a second expanding part. It is interesting to observe that for all values of S_r^d chosen, the solution settles down to the same values of $S_a \approx 0.847$ and $S_b \approx 0.365$, see Fig. 7. The solution, μ_{pf}, has a similar structure with uniform states corresponding to $\mu_e(S_a)$ and $\mu_e(S_b)$ with a diffused transition in between.

Akin to the imbibition case, the sharper transitions between S_b and S_a translate self-similarly in space. See, Fig. 9(b) where one of the solutions from Fig. 7 is plotted in the TW-coordinate $\xi = x - ct$, where c is given by Eq. (34) with $S_- = S_b$ and $S_+ = S_a$. The transition region collapses into the vicinity of $\xi = 0$ as expected for the associated shock solution, Eq. (33), which is also plotted. The corresponding TW-solutions of Eq. (31) will be looked for in Section 3.2.2, which are shown to be non-classical in the sense of shocks violating the entropy condition such that Eq. (38).

The expanding parts of the solution in front of and behind the sharper transition do not translate in the same fashion. Under a transformation of variable $\xi = x/t$, the part connecting S_r^d to S_b tends to collapse into the corresponding rarefaction solution, Eq. (36), of the hyperbolic equation, Eq. (32), with $S_- = S_r^d$ and $S_+ = S_b$, see Fig. 9(c). In fact the flux function is convex within the interval $(S_-, S_+) = (S_r^d, S_b) = (0.20, 0.365)$ and since $S_- < S_+$ the rarefaction wave that is observed is expected. On the other hand, it can be observed that for the same transformation the part connecting S_a to S_r^0 does not collapse into a similarity type solution. In fact, the flux function is non-convex within the interval $(S_a, S_r^0) = (0.847, 0.99)$ and so a rarefaction wave with $S_- = S_a$ and $S_+ = S_r^0$ is not an associated weak solution.

At the junction of the expanding part of the solution and the uniform state, S_b, longitudinal oscillations are observed which seem to grow with time, see Fig. 7. It is explained in Section 3.2.2 with the help of dynamical systems analysis that these oscillations are triggered due to the nature of the equilibrium state associated to S_b. The growth of such oscillations with time on the other hand, is justified in Part II of the current study by analyzing the linear stability of one-dimensional uniform saturation states against longitudinal perturbations.

The overall solution structure represents a drainage scenario in which ahead of the macroscopic air–water interface, the air phase can start invading the pores. And behind such interface there exists an uniform saturation state of the water phase corresponding to S_b, that is not displaced.

Now, for $S_r^d = 0.20$, we vary λ, see Fig. 8. For lower values of $\lambda = 0.5\rho_w g, 1.5\rho_w g$, and thus of C_a, the solution structure is similar to that of $\lambda = \rho_w g$ with two intermediate uniform states S_a and S_b appearing at later times. However, for relatively higher values of $\lambda = 150\rho_w g$, $1500\rho_w g$ a single uniform state, $S_b \approx 0.797, 0.791$ respectively, appears which connects to the right directly to S_r^0 through a sharper transition representing the air–water front. This intermediate state, S_b, connects

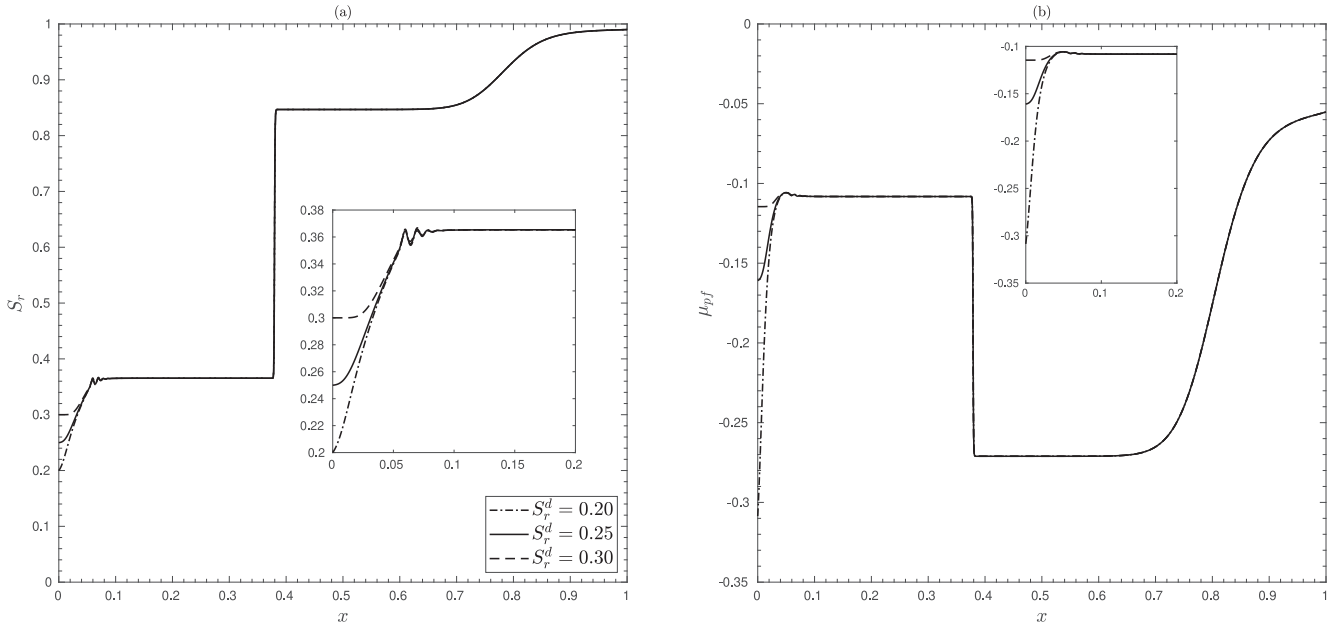

Fig. 7. One dimensional drainage solutions of the coupled system Eq. (41), for $\lambda = \rho_w g$, with initial condition $S_r^0 = 0.99$ and boundary conditions corresponding to drainage reaching $S_r^d = 0.20, 0.25, 0.30$ in $t_d = 100\Delta t$, with Δt = 1E-05, Δx = 5E-04, (a) Saturation degree, S_r, with the pair of intermediate states $(S_a, S_b) \approx (0.847, 0.365)$, (b) regularized effective chemical potential, μ_{pf}. Solutions are shown at the same time-step. Insets focus on the oscillatory junction between the bottom rarefaction wave and the uniform solution state (a) $S_b \approx 0.365$, (b) $\mu_e(S_b)$.

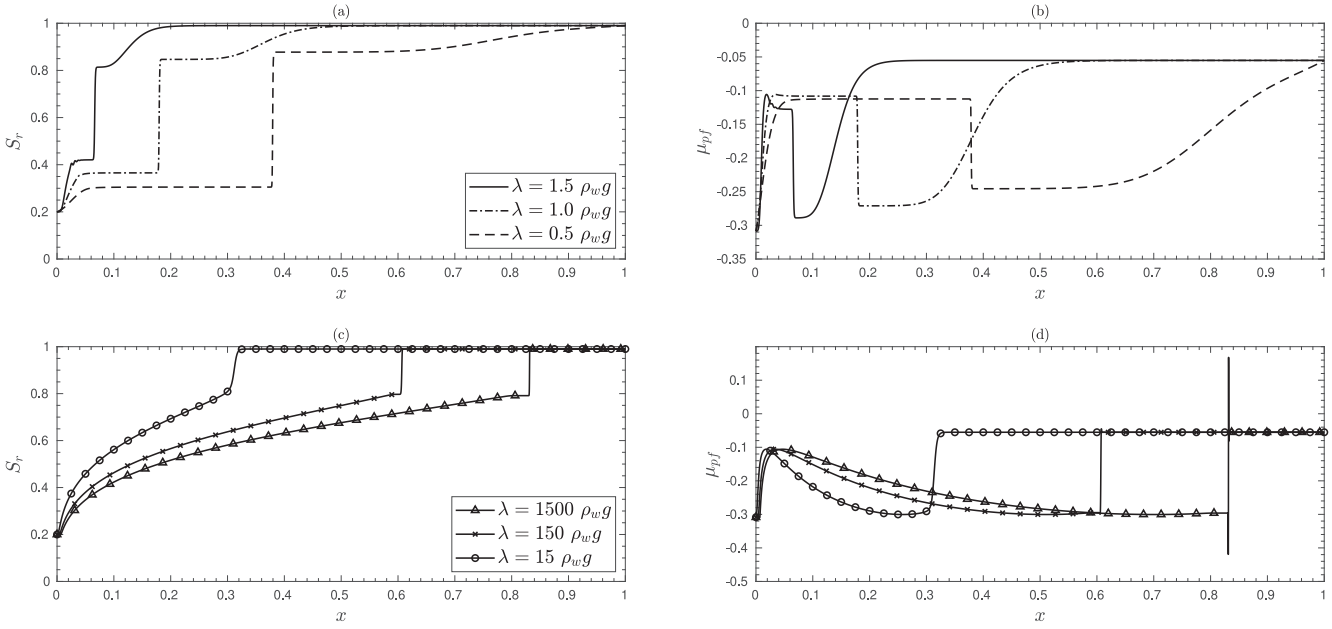

Fig. 8. One dimensional drainage solutions of the coupled system Eq. (41), with initial condition $S_r^0 = 0.99$ and boundary conditions corresponding to drainage reaching $S_r^d = 0.20$, in $t_d = 100\Delta t$, with $\lambda = 0.5\rho_w g, \rho_w g, 1.5\rho_w g$, Δt = 1E-05, Δx = 5E-04, (a) Saturation degree, S_r, with pairs of intermediate states, in the same order as that of λ values, $(S_a, S_b) \approx (0.878, 0.305), (0.847, 0.365), (0.814, 0.421)$, (b) regularized effective chemical potential, μ_{pf}; And with $\lambda = 15\rho_w g, 150\rho_w g, 1500\rho_w g$, Δt = 1E-06, Δx = 1E-04, (c) Saturation degree, S_r, with the intermediate states $S_b \approx 0.797, 0.791$ for $\lambda = 150\rho_w g, 1500\rho_w g$ respectively, (d) regularized effective chemical potential, μ_{pf}; Solutions are shown at different time-steps for clarity.

to S_r^d to the left through an expanding part. The regularized effective chemical potential, μ_{pf}, follows a similar structure in accordance with Eq. (20).

A transformation into the TW-coordinate $\xi = x - ct$, where c is given by Eq. (34) with $S_- = S_b$ and $S_+ = S_r^0$ reveals the self-similar nature of the sharper transition, see Fig. 10(b). In Section 3.2.2 the corresponding TW-solutions of Eq. (31) will be looked which are also non-classical in the sense of shocks violating the entropy condition such that Eq. (37). Whereas under a transformation of variable $\xi = x/t$, the part connecting S_r^d to S_b tends to collapse into the corresponding rarefaction solution, Eq. (36), of the hyperbolic equation, Eq. (32), with $S_- = S_r^d$ and $S_+ = S_b$, see Fig. 10(c).

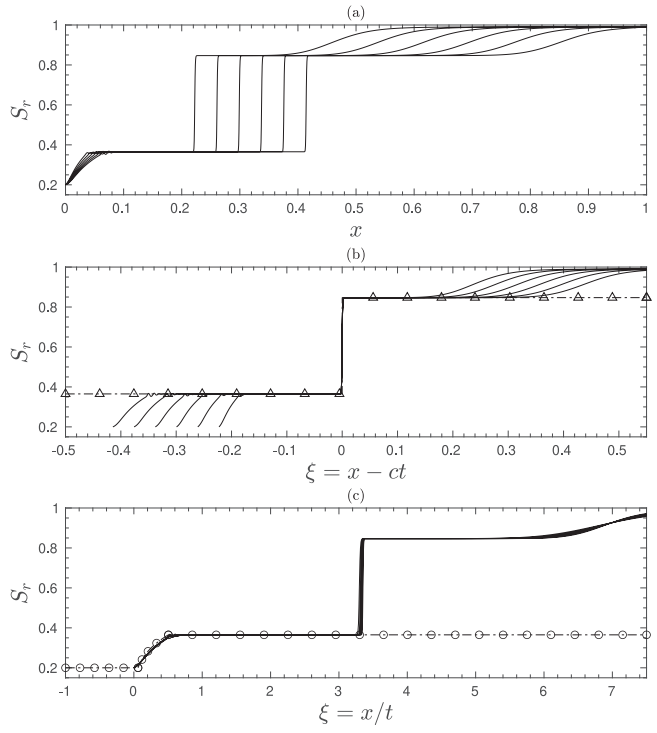

Fig. 9. One dimensional drainage solution S_r of the coupled system Eq. (41), for $\lambda = \rho_w g$, $S_r^0 = 0.99$ and $S_r^d = 0.20$; (a) Solution at various time steps, (b) Solutions in (a) transformed into the TW-coordinate $\xi = x - ct$ with $c \approx 3.41$ given by Eq. (34). Shock solution, Eq. (33), for $S_- = S_b \approx 0.365$ and $S_+ = S_a \approx 0.847$ is shown with triangle markers, (c) Solutions in (a) transformed into the coordinate $\xi = x/t$. Rarefaction solution, Eq. (36), for $S_- = S_r^d$ and $S_+ = S_b \approx 0.365$ is shown in circle markers.

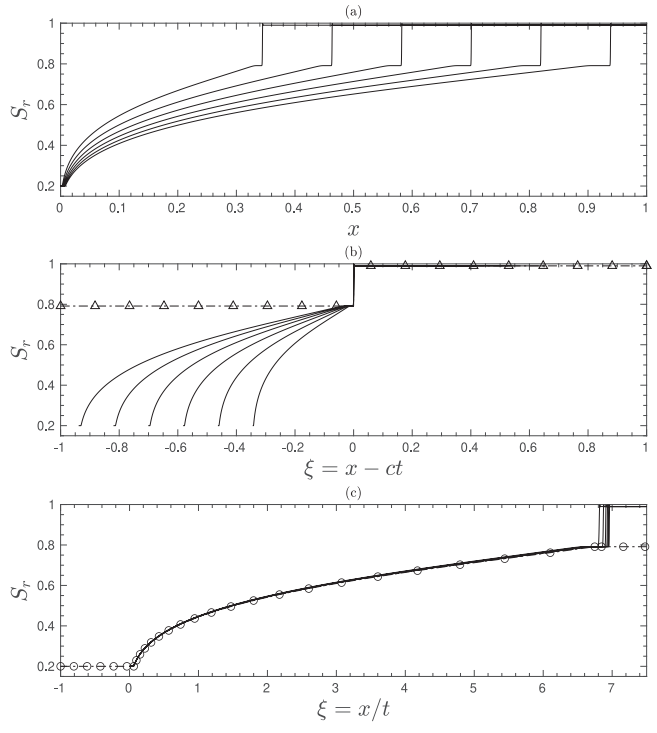

Fig. 10. One dimensional drainage solution S_r of the coupled system Eq. (41), for $\lambda = 1500\rho_w g$, $S_r^0 = 0.99$ and $S_r^d = 0.20$; (a) Solution at various time steps, (b) Solutions in (a) transformed into the TW-coordinate $\xi = x - ct$ with $c \approx 7.05$ given by Eq. (34). Shock solution, Eq. (33), for $S_- = S_b \approx 0.791$ and $S_+ = S_r^0 = 0.99$ is shown with triangle markers, (c) Solutions in (a) transformed into the coordinate $\xi = x/t$. Rarefaction solution, Eq. (36), for $S_- = S_r^d$ and $S_+ = S_b \approx 0.791$ is shown in circle markers.

3.2. Traveling wave analysis

In this section we intend to resolve the TW part of the solutions observed in Section 3.1. With this intent we make a transformation of the independent variables into a moving coordinate,

$$S_r(x,t) = s(x - ct) = s(\xi) \qquad \forall x \in \mathbb{R}\ ;\ \forall t > 0. \tag{45}$$

Where the TW-solution, $s(\xi)$, and speed, c, are a priori not known. The TW-coordinate, ξ, is assumed to have the same speed as that of a shock representative of the transition within the solution $S_r(x,t)$. And so the TW-solution is independent of time and the transition within it is always centered at $\xi = 0$. Introducing Eq. (45) into Eq. (31) yields an ordinary differential equation (ODE) that $s(\xi)$ needs to satisfy:

$$\begin{aligned} -\phi c \frac{ds}{d\xi} + \frac{dK(s)}{d\xi} - \frac{\delta_R}{C_a}\frac{d}{d\xi}\left(K(s)\mu_e'(s)\frac{ds}{d\xi}\right) \\ + \frac{\delta_R}{C_a}\phi D_{NL}\frac{d}{d\xi}\left(K(s)\frac{d^3 s}{d\xi^3}\right) = 0, \end{aligned} \tag{46}$$

The existence of such traveling wave type similarity solutions for Eq. (31) can qualitatively explain part of the complete saturation solution, $S_r(x,t)$, ranging between the two uniform states (see figures in Section 3.1). In other words the TW-solution, $s(\xi)$, of Eq. (46) can represent a branch of the PDE solution $S_r(x,t)$, with the corresponding boundary conditions on an infinite domain:

$$\begin{aligned} s\Big|_{(\xi=+\infty)} &= s_+\ , \quad \frac{ds}{d\xi}\Big|_{(\xi=+\infty)} = 0, \\ s\Big|_{(\xi=-\infty)} &= s_-\ , \quad \frac{ds}{d\xi}\Big|_{(\xi=-\infty)} = 0. \end{aligned} \tag{47}$$

Integrating Eq. (46) once w.r.t ξ, using the boundary conditions at $\xi = +\infty$ and assuming higher derivatives of the solution vanish as $\xi \to +\infty$ yields in a canonical form:

$$\begin{aligned} \frac{d^3 s}{d\xi^3} = \frac{C_a}{\delta_R \phi D_{NL} K(s)}\Bigg(\phi c(s - s_+) - K(s) + K(s_+) \\ + \frac{\delta_R}{C_a} K(s)\mu_e'(s)\frac{ds}{d\xi}\Bigg). \end{aligned} \tag{48}$$

The Rankine–Hugoniot jump condition, Eq. (34), for the speed, c, of the representative shock can be recovered by employing Eq. (47) as $\xi \to -\infty$. Since we are looking for TW-solutions satisfying boundary conditions Eq. (47), the states s_- and s_+ are two known equilibria of Eq. (48). In order to analyze their properties and the possibility of existence of other such equilibria it is convenient to rewrite Eq. (48) into a system of first order ODEs:

$$\begin{aligned} s_\xi &= v, \\ v_\xi &= w, \\ w_\xi &= \frac{C_a\left(\phi c(s - s_+) - K(s) + K(s_+)\right)}{\delta_R \phi D_{NL} K(s)} + \frac{\mu_e'(s)}{\phi D_{NL}} v. \end{aligned} \tag{49}$$

In the above sub-script ξ is used to represent derivative of a variable w.r.t to ξ. In the sense of a dynamical system with ξ playing the role of a time-like independent variable, the TW-solutions can viewed as trajectories connecting associated equilibria, $(s_e, 0, 0)$, of such system. The local stability properties of such equilibria determine the nature of the connection between them, (Bertozzi and Shearer, 2000). The eigen values of a corresponding linearized system in the vicinity of an equilibrium reveals the behavior of a small perturbation to it. These eigen values are the roots of the depressed cubic equation,

$$\beta^3 - \frac{\mu_e'(s_e)}{\phi D_{NL}}\beta - \frac{C_a\left(\phi c - K'(s_e)\right)}{\delta_R \phi D_{NL} K(s_e)} = 0. \tag{50}$$

A detailed deduction of the above linearization is done in Appendix A. According to the classical Cardano–Tartaglia formula for roots of depressed cubic equations, for $\mu_e'(s_e) > 0$, if the discriminant of Eq. (50)

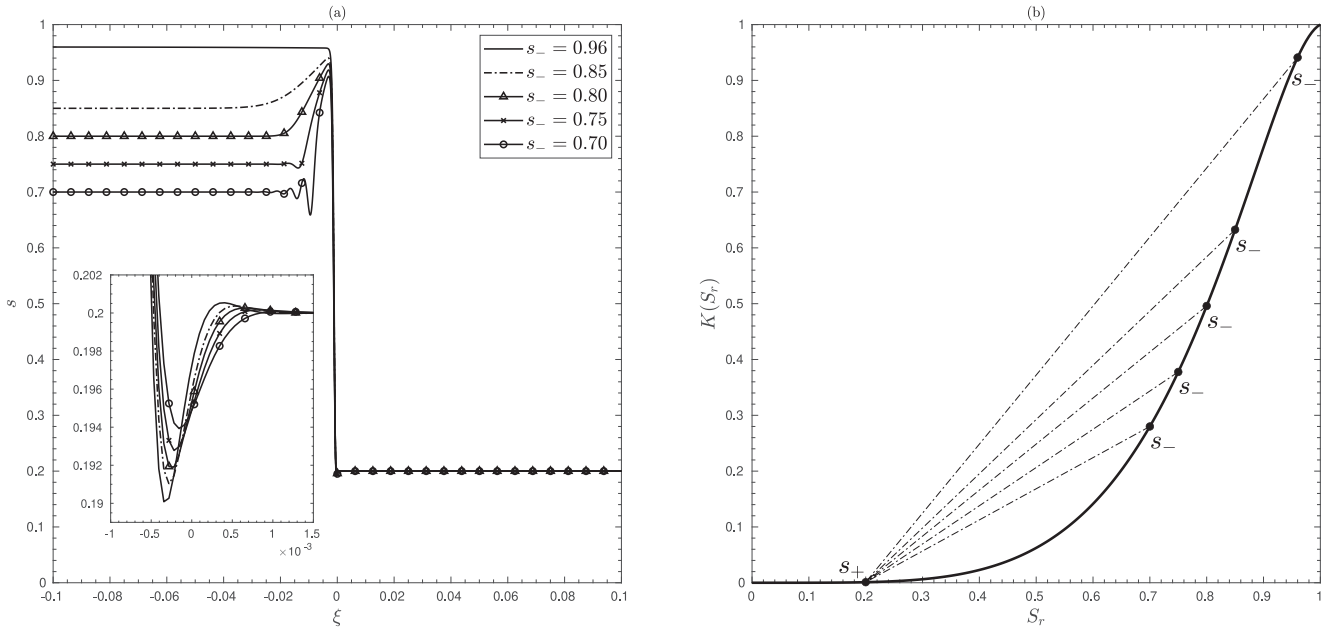

Fig. 11. (a)TW-solutions of Eq. (48) for $\lambda = \rho_w g$, with boundary conditions $s_+ = 0.20$, $s_- = 0.96, 0.85, 0.80, 0.75, 0.70$. Solutions are shown in a restricted range of ξ for clarity. (b) the corresponding connections shown on the curve $K(S_r)$.

is negative, then all three eigen values corresponding to the equilibrium are real. This condition can be simplified to,

$$\frac{C_a\sqrt{\phi D_{NL}}}{\delta_R}\frac{(\phi c - K'(s_e))}{K(s_e)} < \left(\frac{4}{27}(\mu_e'(s_e))^3\right)^{\frac{1}{2}}. \tag{51}$$

Else, only one eigen value of the three is real and the other two are complex conjugates giving rise to oscillatory behavior in the vicinity of such equilibria. On the other hand, for a $\mu_e'(s_e) < 0$, one eigen value of the three is real and other two are complex conjugates, irrespective of the sign of the discriminant. These relations form the basis for understanding the behavior of TW-solutions in the vicinity of their respective equilibrium states, $(s_e, 0, 0)$.

3.2.1. Imbibition

As observed in Section 3.1.1, the imbibition solutions are self-similar in the whole of the domain such that the uniform saturation states observed in the PDE solutions correspond to the imposed boundary conditions, S_-, on the left and initial conditions, S_r^0, on the right. Hence, saturation states at the boundaries of TW-solutions in Eq. (47) are chosen as $s_+ = S_r^0$ and $s_- = S_-$. And then the third order ODE Eq. (48) is numerically resolved over a domain of finite physical length, $L = 100$m, that is sufficiently large in comparison to the characteristic interface thickness, ℓ, such that we get a satisfactory approximation of an unbounded domain. Within this domain, the transition region from s_- to s_+ would be centered at $\xi = 0$. We discretize this domain using an uniform finite difference grid and use a second order accurate central difference scheme to approximate the derivatives in Eq. (47) and (48). Then the solutions are obtained solving the non-linear problem starting from an initial guess that is a sharp transition at $\xi = 0$ between the intended saturation values on either side.

Fig. 11 shows these solutions and their corresponding transitions as connections on the graph of flux function, $K(S_r)$, for various values of s_- and $\lambda = \rho_w g$. The slope of these connections is the speed, c, of the corresponding shock that is represented by the TW-solution. As can be inferred from the plot, the relation between characteristic speed on either side of the connection, $K'(s_-)$, $K'(s_+)$, and the speed of the shock is such that these connections are representative of classical compressive shocks that satisfy the Lax entropy condition, Eq. (35). Moreover, similar to observations made in Section 3.1.1, there exist non-monotonicities of overshoot type and oscillatory type. These solutions are qualitatively comparable to the results of one-dimensional experiments done by DiCarlo (2004) for constant rate infiltration of water into initially dry sand. In those experiments, while for the highest imposed flux the water saturation profile was monotonic, for intermediate fluxes non-monotonicities were observed, which grew stronger as the flux is lowered within the intermediate range. It can observed in Fig. 11 the same trend as in the experiments, of the non-monotonicities with respect to varying flux, Eq. (43).

In order to aid the analysis of the behavior in the vicinity of equilibria, $(s_-, 0, 0)$ and $(s_+, 0, 0)$, these TW-solutions understood as trajectories running between the equilibria are plotted, see Fig. 12, in the phase space governed by the third order ODE system Eq. (49). For all s_- the solution close to s_+ is oscillatory. However, behind the front, for certain values of $s_- = 0.85, 0.80$, there is a non-oscillatory overshoot and for $s_- = 0.75, 0.70$ the overshoot is oscillatory as it leaves the equilibrium at s_-. For $s_- = 0.96$ there is neither an overshoot nor oscillations behind the front.

The oscillatory behaviors at both the equilibria can be explained analyzing the corresponding linearized eigen values. For all left equilibrium states, $(s_-, 0, 0)$, such that $\mu_e'(s_-) < 0$ results in oscillations, when leaving this state as seen in the case of $s_- = 0.75, 0.70$. The right equilibrium state, $(s_+ = 0.20, 0, 0)$, is such that $\mu_e'(s_+) > 0$. However, the condition on discriminant being negative, Eq. (51), is not satisfied for the choice of C_a and D_{NL} resulting in oscillations when arriving $s_+ = 0.20$.

The overshoot behavior on the other hand can be explained by employing singular perturbation techniques (Witelski, 1996). To do this we introduce a small nonzero parameter, $\epsilon \approx O(\ell/x_h)$, and expand the solution using a perturbation series, $s(\xi) = s_0(\xi) + \epsilon s_1(\xi) + \epsilon s_2(\xi)\dots$, which separates Eq. (46) into a cascade of problems each governing the solution at a particular order. As $\epsilon \to 0$ the leading order solution, $s_0(\xi)$, is governed by

$$-\phi c\frac{ds_0}{d\xi} + \frac{dK(s_0)}{d\xi} - \frac{\delta_R}{C_a}\frac{d}{d\xi}\left(K(s_0)\mu_e'(s_0)\frac{ds_0}{d\xi}\right) = 0. \tag{52}$$

Integrating once w.r.t ξ and employing boundary conditions, Eq. (47), at $\xi = +\infty$ gives,

$$-\phi c(s_0 - s_+) + K(s_0) - K(s_+) - \frac{\delta_R}{C_a}K(s_0)\mu_e'(s_0)\frac{ds_0}{d\xi} = 0. \tag{53}$$

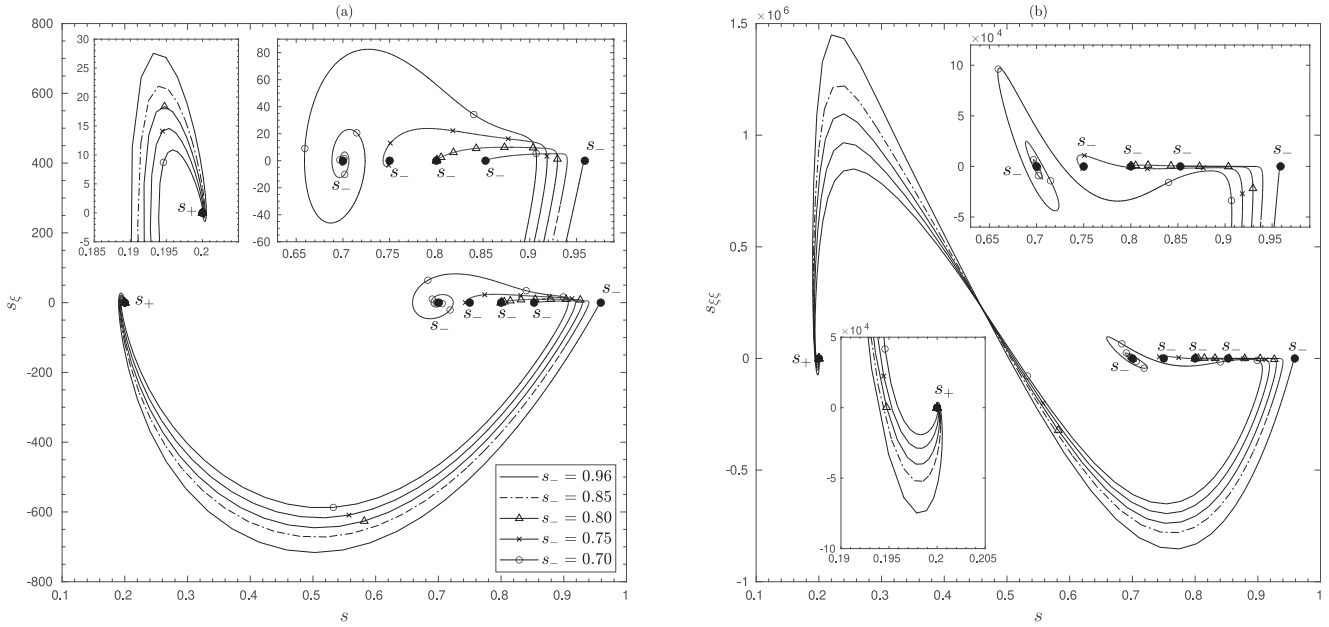

Fig. 12. TW-solutions shown as trajectories in the phase space defined by of Eq. (49) for $\lambda = \rho_w g$, with boundary conditions $s_+ = 0.20$, $s_- = 0.96, 0.85, 0.80, 0.75, 0.70$; phase plane views (a) (s, s_ξ), (b) $(s, s_{\xi\xi})$.

This results in a smooth implicit solution valid outside the transition zone and so-called the 'outer' solution:

$$\begin{aligned}\xi(s_0) - \xi_m &= \int_{\xi_m}^{\xi} d\Xi \\ &= \int_{s_m}^{s_0} \frac{\frac{\delta_R}{C_a} K(S)\mu_e'(S)}{-\phi c(S - s_+) + K(S) - K(s_+)} dS,\end{aligned} \tag{54}$$

where ξ_m is a reference value, chosen to be 0.0, at which an arbitrary $s_m \in (s_+, s_-)$, chosen to be 0.5, occurs. This implicit solution is plotted in Fig. 13 for values $s_- = 0.96, 0.85$ and $s_+ = 0.20$. It is clear that in both cases the solution is non-monotonic in ξ for a range of s_0 within (s_+, s_-) and thus non-physical. Whereas, the parts of the solution for s_0 within $(s_-, 1.0)$ and (S_r^{res}, s_+) increase monotonically with s_0. Now, in order to resolve the non-physicality a weak solution can be constructed by traversing the non-physical region with a discontinuity. However, this jump in the saturation degree needs to comply with a continuity in the pressure whose gradient should exist. This condition can be met in the current model thanks to the double-well structure of the energy density which as explained earlier gives rise to isopotential saturation states. For the choice of parameters in the current study these isopotential states can be obtained as $(S_1^c, S_2^c) \approx (0.91, 0.23)$ using Maxwell construction. Now, exploiting the translational invariance of the implicit solution, Eq. (54), a weak implicit solution of the following form can be built using (S_1^c, S_2^c):

$$\widehat{\xi}(s_0) - \xi_m = \begin{cases} \xi(s_0) - \xi(S_1^c), & \forall \widehat{\xi} < \xi_m, \\ \xi(s_0) - \xi(S_2^c), & \forall \widehat{\xi} > \xi_m. \end{cases} \tag{55}$$

It is to be noted that the choice of boundary conditions on saturation degree, (s_-, s_+), is independent of the isopotential saturation states determined (S_1^c, S_2^c). Thus a combination of solutions is possible and accordingly the appropriate part of the outer solution, Eq. (54), needs to be chosen to further translate and construct the weak outer solution, Eq. (55). For instance, if $s_- > S_1^c$ and $s_+ < S_2^c$ the part of outer solution, $\xi(s_0)$, that is to be translated in the construction of $\widehat{\xi}(s_0)$ is the non-monotonic part within (s_+, s_-). See for example the case of $s_- = 0.96$ in Fig. 13(a). On the other hand if $s_- < S_1^c$ and $s_+ < S_2^c$, the monotonically increasing outer solution, $\xi(s_0)$, within $(s_-, 1.0)$ is shifted to the right giving $\xi(s_0) - \xi(S_1^c)$, and the non-monotonic part within (s_+, s_-) is shifted to the right giving $\xi(s_0) - \xi(S_2^c)$. See the case of $s_- = 0.85$ in Fig. 13(b). The jump part of the weak implicit solutions thus constructed traversing the non-physical zone can be seen as dotted vertical lines in Fig. 13. In this manner the presence of overshoots in the PDE solutions in Section 3.1.1 and in the TW-solutions can be rationalized comparing the left end boundary condition of saturation with the isopotential saturation state closest to it, S_1^c. Similarly two other combinations of solutions can be envisaged when $s_+ > S_2^c$, which involve undershoot when connecting to equilibrium state at s_+.

On the other hand, the structure of the 'inner' transition region can be resolved by making a transformation into a stretched variable, $\tilde{\xi} = (\xi - \xi_m)/\epsilon$, thus restricting the problem into the transition region. Under such transformation and further expanding the resulting solution, $\tilde{s}$, using a perturbation series w.r.t ϵ allows one to identify the leading order 'inner' problem,

$$-\mu_e'(\tilde{s}_0)\, \frac{d\tilde{s}_0}{d\tilde{\xi}} + \phi \frac{d^3\tilde{s}_0}{d\tilde{\xi}^3} = 0, \tag{56}$$

for $\tilde{s}_0$. Integrating Eq. (56) w.r.t $\tilde{\xi}$ using the boundary conditions that allow appropriate matching of the inner and outer solutions on one side, i.e., $\tilde{s}_0 = S_2^c$ and derivatives of $\tilde{s}_0$ vanish as $\tilde{\xi} \to \infty$, gives the implicit inner solution,

$$\begin{aligned}\tilde{\xi}(\tilde{s}_0) - \tilde{\xi}_m &= \int_{\tilde{\xi}_m}^{\tilde{\xi}} d\tilde{\Xi} \\ &= \int_{\tilde{s}_m}^{\tilde{s}_0} \left[\frac{2}{\phi} \int_{S_2^c}^{\tilde{s}_0} \left(\mu_e(\tilde{S}) - \mu_e(S_2^c)\right) d\tilde{S} \right]^{-\frac{1}{2}} d\tilde{S},\end{aligned} \tag{57}$$

where $\tilde{\xi}_m = 0$ is a reference value where an arbitrary $\tilde{s}_m = 0.5$ is chosen to occur. This inner solution approaches smoothly on the other side, $\tilde{\xi} \to -\infty$, to $\tilde{s}_0 = S_1^c$, see Fig. 14. Thus the leading order inner solution is affected neither by the form of flux function, $K(s)$, nor by the boundary conditions chosen, Eq. (47). Once the implicit solutions Eq. (55) and (57) are determined, a solution valid over the full domain can be constructed using asymptotic matching techniques with appropriate

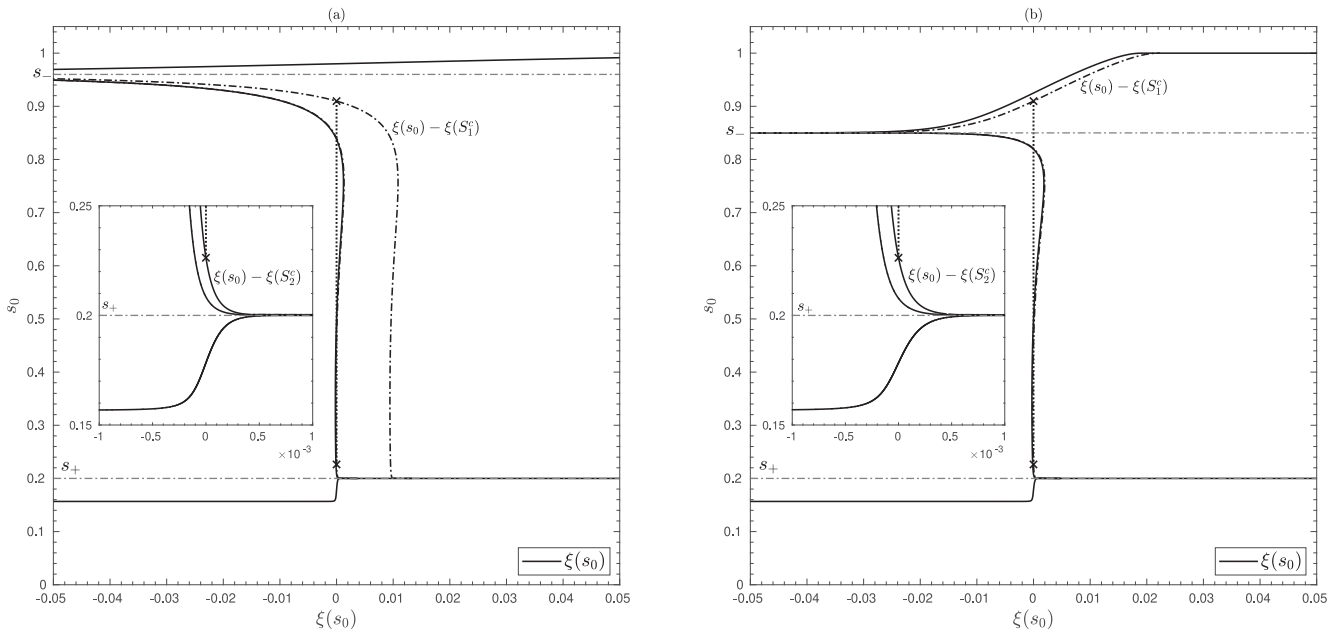

Fig. 13. Implicit outer solutions, Eq. (54), shown as solid lines. Corresponding shifted solutions, $\xi(s_0) - \xi(S_1^c)$ and $\xi(s_0) - \xi(S_2^c)$, shown as dot-dashed lines. The jump part within the weak solution Eq. (55) shown as dotted connection between points $(0, S_1^c)$ and $(0, S_2^c)$ which are shown as crosses. Boundary conditions shown as dot-dashed horizontal reference lines for (a) $(s_-, s_+) = (0.96, 0.20)$, (b) $(s_-, s_+) = (0.85, 0.20)$. Solutions are shown in a restricted range of ξ for clarity.

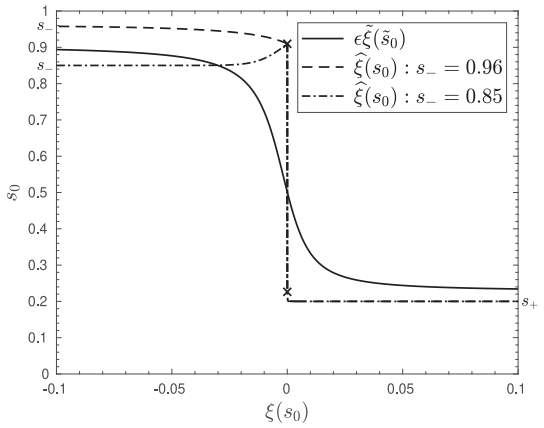

Fig. 14. Implicit inner solution, Eq. (57), scaled back from the stretched variable space, $\epsilon\tilde{\xi}(\tilde{s}_0)$, shown as a solid line in the space $(\xi(s_0), s_0)$. This solution varies between $S_1^c \approx 0.91$ and $S_2^c \approx 0.23$. The weak implicit outer solution, Eq. (55), is shown for both the boundary conditions $(s_-, s_+) = (0.96, 0.20)$ (dashed) and $(s_-, s_+) = (0.85, 0.20)$ (dot-dashed). These involve a jump between $(0, S_1^c)$ and $(0, S_2^c)$ which are shown as crosses. Solutions are shown in a restricted range of ξ for clarity.

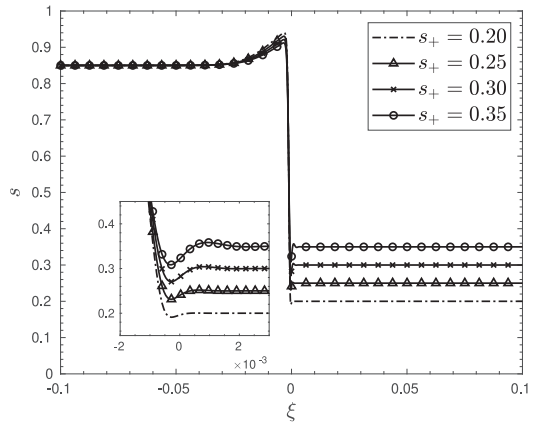

Fig. 15. TW-solutions of Eq. (48) representing imbibition for $\lambda = \rho_w g$, with boundary conditions $s_+ = 0.20, 0.25, 0.30, 0.35$, $s_- = 0.85$; Solutions are shown in a restricted range of ξ for clarity.

assumption on the region of overlap of those solutions. One of such possible assumptions involves an uniform matching,

$$s(\xi) = \begin{cases} \widehat{s}_0(\xi) + \tilde{s}_0(\xi) - S_1^c, & \forall \xi < \xi_m, \\ \widehat{s}_0(\xi) + \tilde{s}_0(\xi) - S_2^c, & \forall \xi > \xi_m. \end{cases} \tag{58}$$

In the Eq. (58) above, $\widehat{s}_0(\xi)$ is the inverse mapping of $\widehat{\xi}(s_0)$ in Eq. (55), with an abuse of notation replacing $\widehat{\xi}$ with ξ noting that both take values from the real number line. $\tilde{s}_0(\xi)$ is the inverse mapping of the implicit inner solution that is scaled back from the stretched variable space, $\epsilon\tilde{\xi}(\tilde{s}_0)$. The accuracy of such solutions depends on the assumptions involved in the asymptotic matching procedure.

While, the weak implicit outer solution, Eq. (55), indicates whether the overshoot and undershoot behaviors are to be expected or not in the numerical solutions, it is prudent to note that the integrand in Eq. (54) diverges to $-\infty$ while approaching both s_- and s_+. And this is irrespective of the relation between s_- and s_+, i.e., either $s_- > s_+$ or $s_- < s_+$. Thus integrating backwards from $s_m \in (s_+, s_-)$ to $\min(s_+, s_-)$ always implies $\xi(s_0) \to \infty$ and integrating forwards from $s_m \in (s_+, s_-)$ to $\max(s_+, s_-)$ always implies $\xi(s_0) \to -\infty$. So, this implicit outer solution, is only representative of imbibition solutions and as such drainage solutions are not possible in the context of the leading order outer problem, Eq. (52). As we will see further, it is the second gradient term of the energy that is absent in the outer problem which is responsible for drainage solutions when $K(S_r)$ is non-convex.

With respect to imbibition, s_+ represents the initial saturation condition of the porous media into which injection of fluid is done with a velocity corresponding to s_- of the form Eq. (43). Fig. 15 shows the effect of different initial conditions, s_+, for fixed $\lambda = \rho_w g$ and left boundary condition, $s_- = 0.85$. For larger values of s_+, the oscillatory non-monotonicity ahead of the interface are stronger and more spread-out along ξ, whereas the overshoot behind the interface tends to reduce slightly.

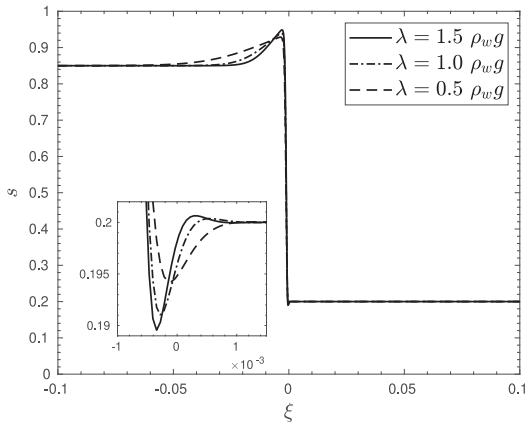

Fig. 16. TW-solutions of Eq. (48) representing imbibition for $\lambda = 0.5\rho_w g, \rho_w g, 1.5\rho_w g$, with boundary conditions $s_+ = 0.20$, $s_- = 0.85$; Solutions are shown in a restricted range of ξ for clarity.

Fig. 16 shows the imbibition solutions for various values of λ and for fixed boundary conditions, $s_- = 0.85, s_+ = 0.20$. Increasing λ tends to result in a reduced spread along ξ of the non-monotonicities within both behind and ahead of the interface. Also, the strength of these non-monotonicities tends to increase with λ.

3.2.2. Drainage

Contrary to the imbibition solutions in Section 3.1, the drainage solutions are not self-similar throughout the domain. Only a part of the solution seems to propagate as traveling waves with uniform intermediate saturation state/s appearing. For lower values of λ two intermediate states S_a and S_b form the traveling wave boundary conditions. And for higher values of λ only one intermediate state S_b connects directly to the initial condition S_r^0. Moreover, these intermediate state/s are not a priori known and hence the boundary conditions to resolve the corresponding TW-solutions are not known. However, it has been shown numerically, in the context of thin film flows, that non-classical 'under-compressive' shocks are unique (Bertozzi et al., 1999; Münch, 2000) in the sense that they represent traveling wave type solutions between unique combination of left and right boundary conditions. Also in the case of lower values of λ in Section 3.1.2, the intermediate states S_a and S_b remained unique irrespective of the changing boundary conditions. Taking cue from these observations, in what follows we consider one of the equilibrium states in the PDE solutions as a known. And then we use an iterative approach to find the unknown equilibrium state, employing a shooting method to integrate forward or backward in ξ, the dynamical system Eq. (49), until the target known equilibrium state is reached.

To do this in the case of lower values of λ we take as input from the 1D PDE results the higher equilibrium state, $(S_a, 0, 0)$, as the target and apply a small perturbation of the order 1E-6 to an initial guess of lower equilibrium state, $(S_b^0, 0, 0)$, in the direction of the eigen vector corresponding to an unstable eigen value at $(S_b^0, 0, 0)$. Then we proceed to integrate forward Eq. (49) using the MATLAB solver-ODE23s (Shampine and Reichelt, 1997) which is based on a modified Rosenbrock method and features adaptive step size. In order to provide stopping criteria for the integration and direction for the iterations we observe two qualitatively different types of trajectories starting from an $(S_b^0, 0, 0)$ in the vicinity of lower equilibrium state obtained in the 1D PDE results, $(S_b, 0, 0)$. See Fig. 17(a). For lower values of S_b^0 the trajectory reaches the target S_a with a positive slope and then diverges towards full saturation. For higher values of S_b^0 on the other hand, it reaches a local maximum missing the target and then moves to a local minimum before diverging to full saturation. The required left equilibrium state would form a trajectory that reaches the target with a zero slope and curvature, up to a numerical error. Assuming such trajectory exists for an S_b^0 within the above two cases, we input them as starting points of iterations in a Regula-Falsi method (Galdino, 2011). The stopping criteria for the iterations is chosen as a tolerance to be satisfied by the difference between the target S_a and the saturation value at which a zero slope achieved. This tolerance is set to 1E-8 in this work. Fig. 17(b) shows the TW-solutions thus obtained for different values of λ and the lower equilibrium state $(S_b^k, 0, 0)$ associated to the last iteration.

For the case of higher λ, where only one intermediate uniform saturation state, S_b, was observed in the 1D PDE results, we follow a similar approach and stopping criteria for the iterations, but with an a priori known target $(S_r^0, 0, 0) = (0.99, 0, 0)$. Again we observe two types of trajectories starting in the vicinity of equilibrium state $(S_b, 0, 0)$. In both cases we observe an oscillatory behavior while approaching the target. See Fig. 17(c). However, for lower values of S_b^0, after oscillation, the trajectory reaches a local minimum without traversing the target and then diverges to full saturation. And for higher values of S_b^0, the trajectory reaches the target S_a with a negative slope and then diverges down towards residual saturation. With these new stopping criteria for integration we obtain TW-solutions shown in Fig. 17(d) for different values of λ.

These drainage TW-solutions are shown as connections on the permeability curve $K(S_r)$ in Fig. 18. The connections for lower values of λ are representative of non-classical 'expansion' shocks that violate Lax entropy condition as Eq. (38). Since these solutions are connections between two equilibria, corresponding local stability properties can be analyzed in accordance with Section 3.2. In the current phase field model these non-classical 'expansion' connections occur between a left equilibrium state, $(s_-, 0, 0)$, which has locally one unstable real eigen value, two stable complex conjugate eigen values and a right equilibrium state, $(s_+, 0, 0)$, which has locally two unstable real eigen values, one stable real eigen value. And hence there are no oscillations observed neither when leaving the left equilibrium state along the unstable eigen vector nor when approaching the right equilibrium state along the stable eigen vector. In Section 3.1.2 it is observed that longitudinal oscillations appear at the junction of a rarefaction wave and the uniform intermediate saturation state associated to S_b. It can be inferred that these oscillations are due to the complex conjugate nature of the stable eigen pair in the vicinity of the left equilibrium state.

On the other hand, the connections for higher values of λ violate Lax entropy condition, Eq. (35), while satisfying the first relation in Eq. (37) and so are representative of non-classical 'under-compressive' shocks which travel faster than the characteristic speed on either side of the shock. For such connections the system governed by Eq. (49) has a third equilibrium, $(s_{e3}, 0, 0)$, such that,

$$\phi c(s_{e3} - s_+) - K(s_{e3}) + K(s_+) = 0. \tag{59}$$

However the solution only represents a connection directly from $(s_-, 0, 0)$ to $(s_+, 0, 0)$ that have the same local stability properties with one unstable real eigen value, two stable complex conjugate eigen values. And the later are responsible for the small oscillatory non-monotonicity when the solution approaches $(s_+, 0, 0)$. See inset in Fig. 17(d).

4. Conclusion

In the current study we have presented a phase field model, as an extension of the classical Richards equation, in order to address the displacement of an air–water interface within a porous medium under the influence of either an imposed pressure gradient and/or gravity. In the framework of thermodynamically consistent phase field modeling (Sciarra, 2016), the air–water mixture in the unsaturated regime was viewed as a non-uniform fluid characterized by a physically motivated phase field parameter, the saturation degree of the wetting fluid (water). While such non-uniform fluid naturally is equipped with

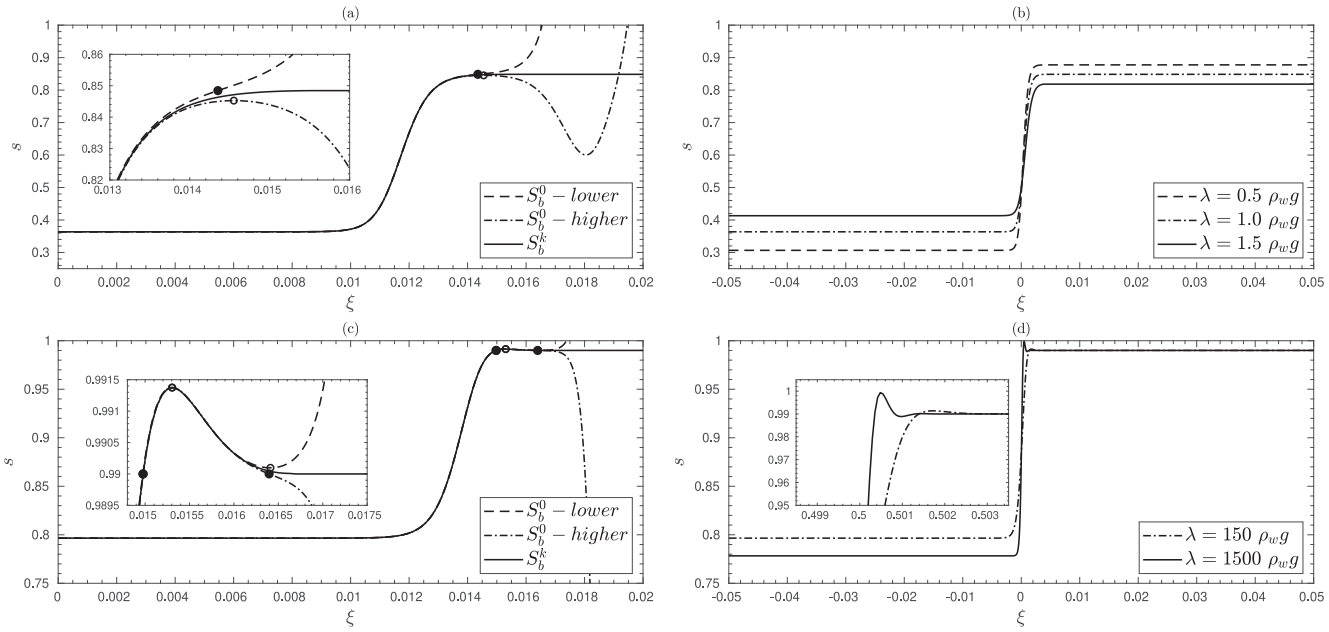

Fig. 17. Trajectories of qualitatively different solutions with lower and higher starting equilibrium states, $(S_b^0, 0, 0)$, for (a) $\lambda = \rho_w g$, (c) $\lambda = 150\rho_w g$. Zero slope locations on the trajectories are shown as circles and locations where the trajectory crosses the target S_a are shown as filled dots. Solid lines represent the solution trajectory at the last iteration starting at equilibrium state $(S_b^k, 0, 0)$. Corresponding TW-solutions centered within the domain $\xi \in [-0.05, 0.05]$, for (b) lower values of $\lambda = 0.5\rho_w g, \rho_w g, 1.5\rho_w g$ for which $(s_-, s_+) = (S_b^k, S_a)$ and $S_b^k \approx 0.30639, 0.36345, 0.413$ respectively with λ and for (d) higher values of $\lambda = 150\rho_w g, 1500\rho_w g$ for which $(s_-, s_+) = (S_b^k, S_r^0)$ and $S_b^k \approx 0.79653, 0.77827$ respectively with λ. Solutions are shown in a restricted range of ξ, s and aspect ratio of insets adjusted for clarity.

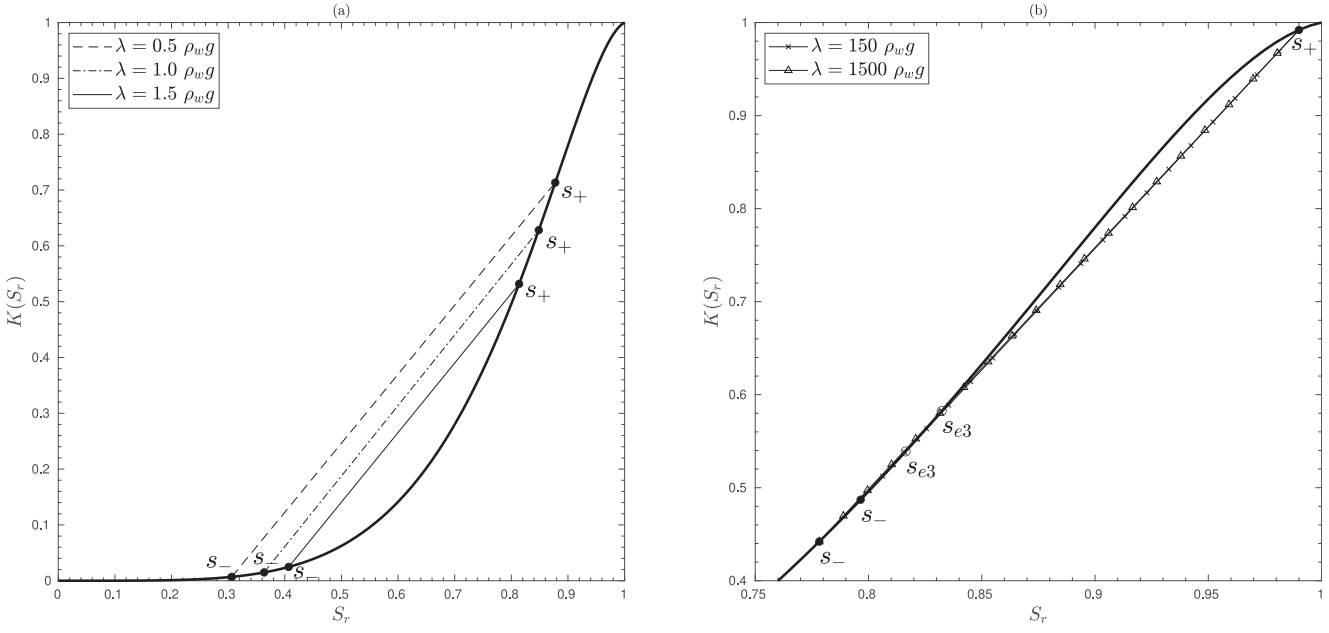

Fig. 18. TW-solutions shown in Fig. 17(b,d) shown as connections on the curve $K(S_r)$ for (a) lower values of $\lambda = 0.5\rho_w g, \rho_w g, 1.5\rho_w g$ for which $(s_-, s_+) = (S_b^k, S_a)$ and for (b) higher values of $\lambda = 150\rho_w g, 1500\rho_w g$ for which $(s_-, s_+) = (S_b^k, S_r^0)$ and $s_{e3} \approx 0.81641, 0.83232$ respectively with λ. The locations of $(s_{e3}, K(s_{e3}))$ on the curve are shown as circle markers.

a bulk and a non-local energy contributions, the confining effect due to the pore walls was assumed to be provided by the classical capillary interfacial energy. The gradient of a chemical potential that is derived from the non-uniform fluid energy was assumed to drive the fluid flow, leading to a generalized Darcy's law. Starting from such a constitutive assumption on the energies and dissipation due to fluid flow, a conservation law has been derived for the non-uniform fluid mass in a non-deformable pore network.

An appropriate dimensional grouping has been proposed and a one-dimensional analysis has been done exploiting the hyperbolic structure

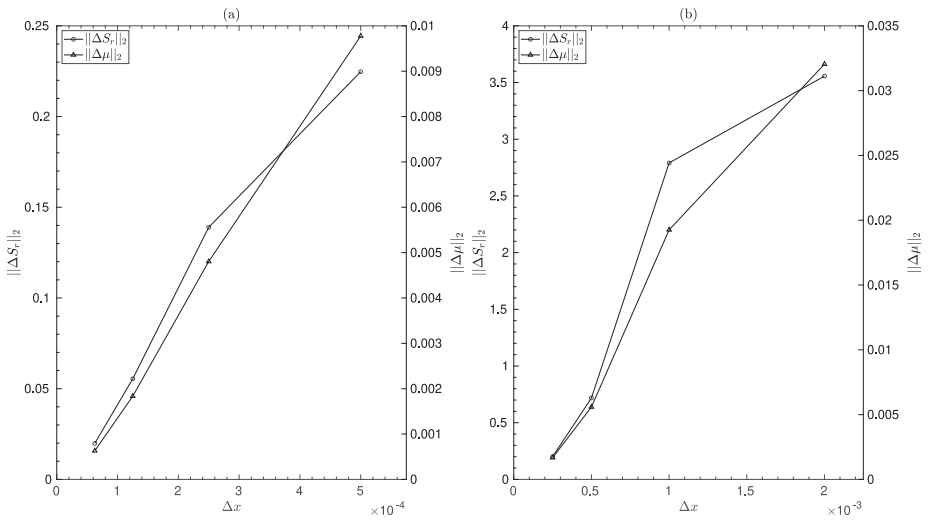

Fig. B.19. Mesh convergence for one-dimensional simulations in Section 3.1 with $\lambda = \rho_w g$, $\Delta x/\Delta t = 50$. $\|\Delta(\cdot)\|_2$ represents the 2-norm of the difference between solutions computed with successive mesh refinements. (a) Imbibition simulations with $S_r^0 = 0.20$, $S_- = 0.80$, Δx = 6.25E-05 1.25E−04 2.5E−04, 5E-04, 1E-03. (b) Drainage simulations with $S_r^0 = 0.99$, $S_r^d = 0.20$, Δx = 2.5E-04, 5E-04, 1E-03, 2E-03, 4E-03.

of the governing conservation law. One-dimensional PDE simulations of the same have informed on the presence of similarity solutions for appropriate initial and boundary conditions. In particular the part of the solution which is a similarity solution of the traveling wave type was understood as the air–water displacement front. As a significant novelty, it has been demonstrated that both imbibition and drainage solutions are possible due to the non-convexity of the proposed flux function. Further with an intent to analyze their linear stability, the part of the solution that is a traveling wave type has been resolved by making a transformation into an appropriate moving coordinate system. These solutions were analyzed by exploiting the underlying dynamical system. The solutions corresponding to imbibition driven by gravity have been found to be non-monotonic under certain boundary conditions and the reason for such non-monotonicities has been analyzed. In the current model, the double-well structure of the non-uniform pore fluid energy has been found to cause overshoot type non-monotonicities depending on the boundary conditions chosen, whereas the oscillatory non-monotonicities are due to the dynamical nature of the equilibria associated to the boundary conditions. The solutions of imbibition under the influence of gravity have shown good qualitative agreement against one-dimensional infiltration experiments, with the trend of the relationship between infiltration flux and saturation degree overshoot being preserved. Drainage solutions connecting unknown boundary conditions as well were resolved using an iterative shooting method starting from left boundary condition taken from the PDE solutions.

In Part II of the current study, these TW-solutions of both imbibition and drainage will be analyzed for their conditional stability against perturbations. A linear stability analysis will be used to investigate the range of wave numbers for which such perturbations grow in time and the effect of non-monotonicities within the solutions on the growth of perturbations. Also, equipped with the knowledge on the range of unstable wave numbers, two-dimensional PDE simulations will be done to characterize the non-linear growth of initial perturbations and formation of fingering instabilities.

CRediT authorship contribution statement

Siddhartha H. Ommi: Conceptualization, Methodology, Formal analysis, Data curation, Writing – original draft. **Giulio Sciarra:** Conceptualization, Reviewing, Supervision. **Panagiotis Kotronis:** Conceptualization, Reviewing, Supervision.

Declaration of competing interest

The authors declare that they have no known competing financial interests or personal relationships that could have appeared to influence the work reported in this paper.

Appendix A. Linearization in the vicinity of $(s_e, 0, 0)$

Starting from the system of equations Eq. (49) rewritten as,

$$S_\xi(\xi) = \mathcal{F}(S(\xi)), \tag{A.1}$$

where $S(\xi) = [s, v, w]^T$ and $\mathcal{F}(S(\xi)) = [f(v), g(w), h(s, v)]^T$ is the associated short-hand notation for the right hand side of Eq. (49). The system can then be expanded about an equilibrium $S_e(\xi) = [s_e, 0, 0]^T$ as,

$$S_\xi(\xi) = \mathcal{F}(S_e(\xi)) + D\mathcal{F}(S_e(\xi))\epsilon + D^2\mathcal{F}(S_e(\xi))\frac{\epsilon^2}{2!} + \cdots, \tag{A.2}$$

where $D\mathcal{F}(S_e(\xi))$ and $D^2\mathcal{F}(S_e(\xi))$ represent the Jacobian and Hessian respectively, of $\mathcal{F}(S(\xi))$ evaluated at the equilibrium. Subsequently $\epsilon = [s_\epsilon, v_\epsilon, w_\epsilon]^T$ being a small perturbation in the vicinity of $S_e(\xi)$ allows us to ignore $O(\epsilon^2)$ and higher order terms, leaving us the linear system of equations governing ϵ as,

$$\epsilon_\xi = D\mathcal{F}(S_e(\xi))\epsilon = \begin{bmatrix} 0 & 1 & 0 \\ 0 & 0 & 1 \\ h_s(s_e, 0) & h_v(s_e, 0) & 0 \end{bmatrix} \begin{bmatrix} s_\epsilon \\ v_\epsilon \\ w_\epsilon \end{bmatrix}, \tag{A.3}$$

where,

$$h_s(s_e, 0) = \frac{C_a\left(\phi c - K'(s_e)\right)}{\delta_R \phi D_{NL} K(s_e)}; \quad h_v(s_e, 0) = \frac{\mu_e'(s_e)}{\phi D_{NL}}. \tag{A.4}$$

The characteristic polynomial, $p(\beta)$, whose roots are the eigen values associated with the system Eq. (A.3) is thus given by,

$$p(\beta) = \det[D\mathcal{F}(S_e(\xi)) - \beta\mathbb{I}] = \beta^3 - h_v(s_e, 0)\beta - h_s(s_e, 0). \tag{A.5}$$

Appendix B. Convergence properties of the one-dimensional solutions

In order to validate the robustness of the numerical scheme adopted to solve the one-dimensional problem of Sections 3.1.1 and 3.1.2 a mesh convergence analysis has been conducted for two test cases relative to the imbibition and the drainage problem. As expected reducing

the element size implies a decrease of the 2-norm of the difference between solutions, for the saturation degree and the generalized chemical potential, computed with successive mesh refinements, see Fig. B.19. Data relative to the test cases are reported in the caption of the figure.

References

Ajayi, T., Gomes, J., Bera, A., 2019. A review of CO2 storage in geological formations emphasizing modeling, monitoring and capacity estimation approaches. Pet. Sci. 16 (5), 1028–1063.

Al-Gharbi, M.S., Blunt, M.J., 2005. Dynamic network modeling of two-phase drainage in porous media. Phys. Rev. E 71, 016308.

Andò, E., Hall, S.A., Viggiani, G., Desrues, J., Bésuelle, P., 2012. Grain-scale experimental investigation of localised deformation in sand: a discrete particle tracking approach. Acta Geotech. 7 (1), 1–13.

Bauters, T., DiCarlo, D., Steenhuis, T., Parlange, J.-Y., 2000. Soil water content dependent wetting front characteristics in sands. J. Hydrol. 231–232, 244–254.

Bear, J., 1972. Dynamics of Fluids in Porous Media. Elsevier.

Beljadid, A., Cueto-Felgueroso, L., Juanes, R., 2020. A continuum model of unstable infiltration in porous media endowed with an entropy function. Adv. Water Resour. 144, 103684.

Bertozzi, A., Münch, A., Shearer, M., 1999. Undercompressive shocks in thin film flows. Physica D 134 (4), 431–464.

Bertozzi, A.L., Shearer, M., 2000. Existence of undercompressive traveling waves in thin film equations. SIAM J. Math. Anal. 32 (1), 194–213.

Biot, M., 1972. Theory of finite deformations of pourous solids. Indiana Univ. Math. J. 21, 597–620.

Boyer, F., Lapuerta, C., 2006. Study of a three component Cahn-Hilliard flow model. ESAIM: M2AN 40 (4), 653–687.

Boyer, F., Lapuerta, C., Minjeaud, S., Piar, B., 2009. A local adaptive refinement method with multigrid preconditionning illustrated by multiphase flows simulations. ESAIM: Proc. 27, 15–53.

Brooks, R., Corey, A., 1964. Hydraulic properties of porous media. Hydrol. Pap., Colo. State Univ. 3.

Buckingham, 1907. Studies on the movement of soil moisture. US Dep. Agric., Bureau Soils (38).

Cahn, J.W., Hilliard, J.E., 1958. Free energy of a nonuniform system. I. Interfacial free energy. J. Chem. Phys. 28 (2), 258–267.

Cahn, J.W., Hilliard, J.E., 1959. Free energy of a nonuniform system. III. Nucleation in a two-component incompressible fluid. J. Chem. Phys. 31 (3), 688–699.

Cancès, C., Matthes, D., Nabet, F., 2019. A two-phase two-fluxes degenerate Cahn–Hilliard model as constrained wasserstein gradient flow. Arch. Ration. Mech. Anal. 233, 837–866.

Chen, S., Doolen, G.D., 1998. Lattice boltzmann method for fluid flows. Annu. Rev. Fluid Mech. 30 (1), 329–364.

Chen, Y.-F., Fang, S., Wu, D.-S., Hu, R., 2017. Visualizing and quantifying the crossover from capillary fingering to viscous fingering in a rough fracture. Water Resour. Res. 53 (9), 7756–7772.

Clothier, B.E., Green, S.R., Deurer, M., 2008. Preferential flow and transport in soil: progress and prognosis. Eur. J. Soil Sci. 59 (1), 2–13.

Coussy, O., 2004. Poromechanics. John Wiley & Sons, Ltd.

Coussy, O., 2010. Mechanics and Physics of Porous Solids. John Wiley & Sons, Ltd.

Cueto-Felgueroso, L., Juanes, R., 2009a. A phase field model of unsaturated flow. Water Resour. Res. 45 (10).

Cueto-Felgueroso, L., Juanes, R., 2009b. Stability analysis of a phase-field model of gravity-driven unsaturated flow through porous media. Phys. Rev. E 79, 036301.

Desrues, J., Andò, E., 2015. Strain localisation in granular media. C. R. Phys. 16 (1), 26–36, Granular physics / Physique des milieux granulaires.

DiCarlo, D.A., 2004. Experimental measurements of saturation overshoot on infiltration. Water Resour. Res. 40 (4).

DiCarlo, D.A., 2013. Stability of gravity-driven multiphase flow in porous media: 40 years of advancements. Water Resour. Res. 49 (8), 4531–4544.

DiCarlo, D.A., Juanes, R., LaForce, T., Witelski, T.P., 2008. Nonmonotonic traveling wave solutions of infiltration into porous media. Water Resour. Res. 44 (2).

DiCarlo, D.A., Mirzaei, M., Aminzadeh, B., Dehghanpour, H., 2012. Fractional flow approach to saturation overshoot. Transp. Porous Media 91 (3), 955–971.

DiCarlo, D.A., Seale, L.D., Ham, K., Willson, C.S., 2010. Tomographic measurements of pore filling at infiltration fronts. Adv. Water Resour. 33 (4), 485–492.

Dukler, Y., Ji, H., Falcon, C., Bertozzi, A.L., 2020. Theory for undercompressive shocks in tears of wine. Phys. Rev. Fluids 5, 034002.

Egorov, A.G., Dautov, R.Z., Nieber, J.L., Sheshukov, A.Y., 2003. Stability analysis of gravity-driven infiltrating flow. Water Resour. Res. 39 (9).

El, G.A., Hoefer, M.A., Shearer, M., 2016. Expansion shock waves in regularized shallow-water theory. Proceedings of the Royal Society A: Mathematical, Physical and Engineering Sciences 472 (2189), 20160141.

Eliassi, M., Glass, R.J., 2001. On the continuum-scale modeling of gravity-driven fingers in unsaturated porous media: The inadequacy of the richards equation with standard monotonic constitutive relations and hysteretic equations of state. Water Resour. Res. 37 (8), 2019–2035.

Eliassi, M., Glass, R.J., 2002. On the porous-continuum modeling of gravity-driven fingers in unsaturated materials: Extension of standard theory with a hold-back-pile-up effect. Water Resour. Res. 38 (11), 16–1–16–11.

Eliassi, M., Glass, R.J., 2003. On the porous continuum-scale modeling of gravity-driven fingers in unsaturated materials: Numerical solution of a hypodiffusive governing equation that incorporates a hold-back-pile-up effect. Water Resour. Res. 39 (6).

Galdino, S., 2011. A family of regula falsi root-finding methods.

Gilfillan, S.M., Wilkinson, M., Haszeldine, R.S., Shipton, Z.K., Nelson, S.T., Poreda, R.J., 2011. He and ne as tracers of natural CO2 migration up a fault from a deep reservoir. Int. J. Greenh. Gas Control 5 (6), 1507–1516.

Glass, R.J., Nicholl, M.J., Yarrington, L., 1998. A modified invasion percolation model for low-capillary number immiscible displacements in horizontal rough-walled fractures: Influence of local in-plane curvature. Water Resour. Res. 34 (12), 3215–3234.

Glass, R., Steenhuis, T., Parlange, J.-Y., 1988. Wetting front instability as a rapid and far-reaching hydrologic process in the vadose zone. J. Contam. Hydrol. 3 (2), 207–226, Rapid and Far-Reaching Hydrologic Processes in the Vadose Zone.

Glass, R.J., Yarrington, L., 1996. Simulation of gravity fingering in porous media using a modified invasion percolation model. Geoderma 70 (2), 231–252.

Gray, W.G., Hassanizadeh, S.M., 1991. Unsaturated flow theory including interfacial phenomena. Water Resour. Res. 27 (8), 1855–1863.

Guo, F., Aryana, S.A., 2019. An experimental investigation of flow regimes in imbibition and drainage using a microfluidic platform. Energies 12 (7).

Hassanizadeh, S., Gray, W.G., 1990. Mechanics and thermodynamics of multiphase flow in porous media including interphase boundaries. Adv. Water Resour. 13 (4), 169–186.

Hayes, B., Shearer, M., 1999. Undercompressive shocks and Riemann problems for scalar conservation laws with non-convex fluxes. Proc. R. Soc. Edinburgh A 129 (4), 733–754.

Hilfer, R., Steinle, R., 2014. Saturation overshoot and hysteresis for twophase flow in porous media. Eur. Phys. J. Spec. Top 223 (1), 2323–2338.

Homsy, G.M., 1987. Viscous fingering in porous media. Annu. Rev. Fluid Mech. 19 (1), 271–311.

Hughes, R.G., Blunt, M.J., 2000. Pore scale modeling of rate effects in imbibition. Transp. Porous Media 40 (3), 295–322.

Hughes, R.G., Blunt, M.J., 2001. Network modeling of multiphase flow in fractures. Adv. Water Resour. 24 (3), 409–421, Pore Scale Modeling.

Jacqmin, D., 2000. Contact-line dynamics of a diffuse fluid interface. J. Fluid Mech. 402, 57–88.

Jarvis, N.J., 2007. A review of non-equilibrium water flow and solute transport in soil macropores: principles, controlling factors and consequences for water quality. Eur. J. Soil Sci. 58 (3), 523–546.

Kim, J., 2012. Phase-field models for multi-component fluid flows. Commun. Comput. Phys. 12 (3), 613–661.

Lackner, K.S., 2003. A guide to CO2 sequestration. Science 300 (5626), 1677–1678.

LeFloch, P.G., 2002. Hyperbolic Systems of Conservation Laws. Birkhäuser, Basel, p. X, 294.

Lenormand, R., 1985. Capillary and viscous fingering in an etched network. In: Boccara, N., Daoud, M. (Eds.), Physics of Finely Divided Matter. Springer Berlin Heidelberg, Berlin, Heidelberg, pp. 289–294.

Lenormand, R., 1990. Liquids in porous media. J. Phys.: Condens. Matter 2 (S), SA79–SA88.

Lenormand, R., Touboul, E., Zarcone, C., 1988. Numerical models and experiments on immiscible displacements in porous media. J. Fluid Mech. 189, 165–187.

Leverett, M., 1941. Capillary behavior in porous solids. Trans. AIME 142 (01), 152–169.

Liu, H., Valocchi, A.J., Kang, Q., 2012. Three-dimensional lattice Boltzmann model for immiscible two-phase flow simulations. Phys. Rev. E 85, 046309.

Liu, H., Valocchi, A.J., Werth, C., Kang, Q., Oostrom, M., 2014. Pore-scale simulation of liquid CO2 displacement of water using a two-phase lattice Boltzmann model. Adv. Water Resour. 73, 144–158.

Løvoll, G., Méheust, Y., Måløy, K.J., Aker, E., Schmittbuhl, J., 2005. Competition of gravity, capillary and viscous forces during drainage in a two-dimensional porous medium, a pore scale study. Energy 30 (6), 861–872, Second International Onsager Conference.

Lowengrub, J., Truskinovsky, L., 1998. Quasi-incompressible cahn-hilliard fluids and topological transitions. Proc. R. Soc. Lond. Ser. A Math. Phys. Eng. Sci. 454 (1978), 2617–2654.

Luckner, L., Van Genuchten, M.T., Nielsen, D.R., 1989. A consistent set of parametric models for the two-phase flow of immiscible fluids in the subsurface. Water Resour. Res. 25 (10), 2187–2193.

Macminn, C.W., Szulczewski, M.L., Juanes, R., 2010. Co2 migration in saline aquifers. Part 1. Capillary trapping under slope and groundwater flow. J. Fluid Mech. 662, 329–351.

Majid Hassanizadeh, S., Gray, W.G., 1993. Toward an improved description of the physics of two-phase flow. Adv. Water Resour. 16 (1), 53–67, Research Perspectives in Hydrology.

Martin, D.F., Colella, P., Anghel, M., Alexander, F.L., 2005. Adaptive mesh refinement for multiscale nonequilibrium physics. Comput. Sci. Eng. 7 (03), 24–31.

Méheust, Y., Løvoll, G., Måløy, K.J., Schmittbuhl, J., 2002. Interface scaling in a two-dimensional porous medium under combined viscous, gravity, and capillary effects. Phys. Rev. E 66, 051603.

Morrow, N.R., 1970. Physics and thermodynamics of capillary action in porous media. Ind. Eng. Chem. 62 (6), 32–56.
Münch, A., 2000. Shock transitions in marangoni gravity-driven thin-film flow. Nonlinearity 13 (3), 731–746.
Nieber, J., Bauters, T., Steenhuis, T., Parlange, J.-Y., 2000. Numerical simulation of experimental gravity-driven unstable flow in water repellent sand. J. Hydrol. 231–232, 295–307.
Nieber, J.L., Dautov, R.Z., Egorov, A.G., Sheshukov, A.Y., 2005. Dynamic capillary pressure mechanism for instability in gravity-driven flows; review and extension to very dry conditions. Transp. Porous Media 58 (1), 147–172.
Orr, J., 2004. Storage of carbon dioxide in geologic formations. J. Pet. Technol. 56 (09), 90–97.
Primkulov, B.K., Pahlavan, A.A., Fu, X., Zhao, B., MacMinn, C.W., Juanes, R., 2019. Signatures of fluid–fluid displacement in porous media: wettability, patterns and pressures. J. Fluid Mech. 875, R4.
Primkulov, B.K., Talman, S., Khaleghi, K., Rangriz Shokri, A., Chalaturnyk, R., Zhao, B., MacMinn, C.W., Juanes, R., 2018. Quasistatic fluid-fluid displacement in porous media: Invasion-percolation through a wetting transition. Phys. Rev. Fluids 3, 104001.
Ren, H., Zhuang, X., Trung, N.-T., Rabczuk, T., 2021. Nonlocal operator method for the cahn-hilliard phase field model. Commun. Nonlinear Sci. Numer. Simul. 96, 105687.
Richards, L.A., 1931. Capillary conduction of liquids through porous mediums. Physics 1 (5), 318–333.
Saffman, P.G., Taylor, G.I., 1958. The penetration of a fluid into a porous medium or hele-shaw cell containing a more viscous liquid. Proc. R. Soc. London A 245 (1242), 312–329.
Sciarra, G., 2016. Phase field modeling of partially saturated deformable porous media. J. Mech. Phys. Solids 94, 230–256.
Shampine, L.F., Reichelt, M.W., 1997. The MATLAB ODE suite. SIAM J. Sci. Comput. 18 (1), 1–22.
Shiozawa, S., Fujimaki, H., 2004. Unexpected water content profiles under flux-limited one-dimensional downward infiltration in initially dry granular media. Water Resour. Res. 40 (7).
Song, J., Zhang, D., 2013. Comprehensive review of caprock-sealing mechanisms for geologic carbon sequestration. Environ. Sci. Technol. 47 (1), 9–22, PMID: 23020638.
Torp, T.A., Gale, J., 2004. Demonstrating storage of CO2 in geological reservoirs: The sleipner and SACS projects. Energy 29 (9), 1361–1369, 6th International Conference on Greenhouse Gas Control Technologies.
van Genuchten, M., 1980. A closed-form equation for predicting the hydraulic conductivity of unsaturated soils. Soil Sci. Soc. Am. J. 44, 892–898.
Vardoulakis, I., Goldscheider, M., Gudehus, G., 1978. Formation of shear bands in sand bodies as a bifurcation problem. Int. J. Numer. Anal. Methods Geomech. 2 (2), 99–128.
Witelski, T.P., 1996. The structure of internal layers for unstable nonlinear diffusion equations. Stud. Appl. Math. 97 (3), 277–300.
Xiong, Y., 2014. Flow of water in porous media with saturation overshoot: A review. J. Hydrol. 510, 353–362.
Yamabe, H., Tsuji, T., Liang, Y., Matsuoka, T., 2015. Lattice Boltzmann simulations of supercritical CO2–water drainage displacement in porous media: CO2 saturation and displacement mechanism. Environ. Sci. Technol. 49 (1), 537–543, PMID: 25427299.
Zacharoudiou, I., Boek, E.S., Crawshaw, J., 2018. The impact of drainage displacement patterns and haines jumps on CO2 storage efficiency. Sci. Rep. 8 (1), 2045–2322.
Zhao, J., Yao, J., Li, A., Zhang, M., Zhang, L., Yang, Y., Sun, H., 2016. Simulation of microscale gas flow in heterogeneous porous media based on the lattice Boltzmann method. J. Appl. Phys. 120 (8), 084306.